COO-3158-58

MASTER

DEFECTS IN METAL CRYSTALS

Progress Report

for Period May 1, 1976 - April 30, 1977

David N. Seidman

Cornell University
Ithaca, New York 14853

February 1977

Prepared for

The U.S. Energy Research and Development Administration
under Contract No. EY-76-S-02-3158.*000

DISCLAIMER

DEFECTS IN METAL CRYSTALS

D. N. Seidman

ABSTRACT

The objective of the present research effort is a broad investigation of the properties of crystal defects in metal crystals. Attention during the past year was focused on point defects [vacancies, self-interstitial atoms and solute atoms (both substitutional and interstitial)], aggregates of point defects and their interactions with one another. A strong emphasis was placed on the use of different irradiating species (300-700eV Xe^+ ions, 300eV and 30keV He^+, 20-40keV W^+ ions, 20-40keV Mo^+ ions, 20-40keV Cr^+ ions and fast neutrons) to introduce both vacancies and interstitials in a number of different pure metals (Mo, W, Au, Ta) and alloys [Pt(Au), W(Re), Mo(Ti), Mo(Ti+Zr), Ni_4Mo, Ni_3Fe, Ni_3Mn low-swelling 316 stainless steel and commercial 316 stainless steel].

Progress was made in the following areas:

A. The Study of the Transmission Sputtering of Gold
   1. The experimental measurement of transmission sputtering
   2. Experimental results and discussion

B. Atom-Probe Field-Ion Microscope Studies
   1. Technical improvements in the atom-probe FIM
      a. Automated photographic system
      b. Modified ion gun
   2. Spatial distribution of atomic species in alloys
      a. Tungsten (rhenium) system
      b. Molybdenum (titanium+zirconium) system
      c. Low swelling stainless steel (LSIA)
      d. Neutron irradiated alloys

Key Words: Transmission sputtering; focused replacement collision sequences; energy focusons; gold thin-films; atom-probe field-ion microscopy; spatial distribution of atomic species in neutron irradiated alloys (clustering and anti-clustering); tungsten (rhenium) system; molybdenum (titanium+zirconium) system; low-swelling stainless steel (LSIA); range and mobility of interstitial helium in tungsten; helium bubbles in molybdenum; field-ion microscopy; point-defect structure of depleted zones in ion-irradiated Pt(Au) and tungsten; effect of ion-mass (Cr^+, Mo^+ and W^+ ions) on the spatial distribution of vacancies within a depleted zone;

influence of interstitial nitrogen on self-ion damage in Ta; recovery mechanisms for substages II_B and II_C of ion-irradiated Pt(Au) alloys; range of focused replacement collision sequences in ordered alloys (Ni_4Mo, Ni_3Fe and Ni_3Mn).

I. INTRODUCTION

During the past year a number of projects were completed and significant progress was made in other areas. A brief account of the work is given in Section II. The following personnel were involved:

Professor D. N. Seidman, Principal Investigator
Dr. J. Amano, Research Associate (joined September 1976)
Dr. G. Ayrault, Research Associate (joined October 1973)
Dr. M. Current, Research Associate (joined October 1976)
Dr. T. M. Hall, Research Associate (left July 1976)
J. Aidelberg, Research Assistant (joined September 1974)
J. Kita, Research Assistant (joined June 1976)
I. Sun, Research Assistant (left July 1976)
A. Wagner, IBM Fellowship Holder (joined September 1971)
C. Y. Wei, Research Assistant (joined Septemner 1971)
K. Pratt, Half-time Film Scanner (joined March 1970)
R. Whitmarsh, Technician (joined January 1968)

II. EXPERIMENTAL WORK

A. The Study of the Transmission Sputtering of Gold (Dr. G. Ayrault)

1. The experimental measurement of transmission sputtering

One of the most persistent problems in the field of radiation damage is that of understanding the nature of the initial damage event; i.e., the spatial distribution of vacancies and self-interstitial atoms produced as the result of the impact of an energetic particle. Since Silsbee (1) first introduced the concept of focused collosion sequences (FCS) in 1957, these events have often been discussed as a determining factor in the initial spatial distribution of damage. However, due to experimental difficulties, the range of these events, and even proof of their existence, has remained somewhat elusive. Indeed in gold, FCS ranges of <50A (2) and 4000A or more (3) have been proposed. Clearly, further work is needed to rationalize this immense disparity, and in a more general sense to understand the role of focusing in radiation damage. Toward this end we have developed a unique and direct technique for studying focused collision sequences.

The experiments reported here have been carried out on gold, although the technique should be applicable to other metals as well. The specimens are epitaxially grown, vapor-deposited single crystals with a <100> normal, which range

in thickness from 140 to 500A. A small region of the film [$(2 \text{ to } 8)\times10^{-5}$ cm^2] is irradiated with low-energy ($\leq$700eV) Xe^+ ions directed along the foil normal, as shown in Fig. 1. Focused collision sequences with a range greater than the specimen thickness can cause the ejection of atoms or ions at the bottom foil surface. These are detected using the Bendix Channeltron Electron Multiplier Array (CEMA) system shown in Fig. 1, which consists of two individual CEMAs placed in series. For large signals, the output from the specimen can be detected visually with the aid of a fluorescent screen. For smaller signals and for quantitative measurements, the output is measured electronically.

In order to insure that the observed output from the bottom surface of the specimen is not due to the channeling of light ion impurities (H^+ or He^+) or light energetic neutrals, the crossed electric (E) and magnetic (B) field mass analyzer shown in Fig. 2 is used to remove these components from the Xe^+ beam before it reaches the top surface of the specimen.

The copper specimen mounting block shown in Fig. 2 is attached to the tail section of a continuous transfer liquid helium cryostat, with which the specimen can be maintained at any temperature between $\sim$25 and 300K. The entire apparatus in Fig. 2 (ion gun, mass analyzer, specimen holder and CEMA detection system) is in a high vacuum system ($\sim1\times10^{-7}$ Torr).

In order to achieve the maximum possible detection efficiency, the CEMA system is operated in a saturated mode; a single particle striking it can initiate a cascade of electrons which yields a short pulse ($\sim$10 nsec) of $\sim10^7$ electrons at the fluorescent screen. Using the electronic system shown in Fig. 3 these pulses are individually amplified and shaped into uniform square pulses 1V in amplitude and 10 msec in duration. These are then smoothed for final measurement.

To maximize the signal-to-noise ratio an Ithaco model 391A lock-in amplifier (LIA) is used as the final measuring element. The Xe^+ beam is pulsed at a known frequency ($\sim$100Hz) by pulsing the ion-gun filament bias. This same frequency is used as a reference for the LIA, which then measures only the portion of the CEMA output which is in phase with the ion-current.

Since the output is proportional to the xenon ion current, the quantity of interest is the ratio of the output to input Xe^+ ion current. This ratio is provided directly by a current measuring circuit linked to a ratiometer built into the LIA. Both this ratio R and the direct LIA output are recorded as a function of time on a dual pen strip chart recorder.

Figure 1. Thin film specimen mounting system and CEMA detection system for the study of focused collision sequences.

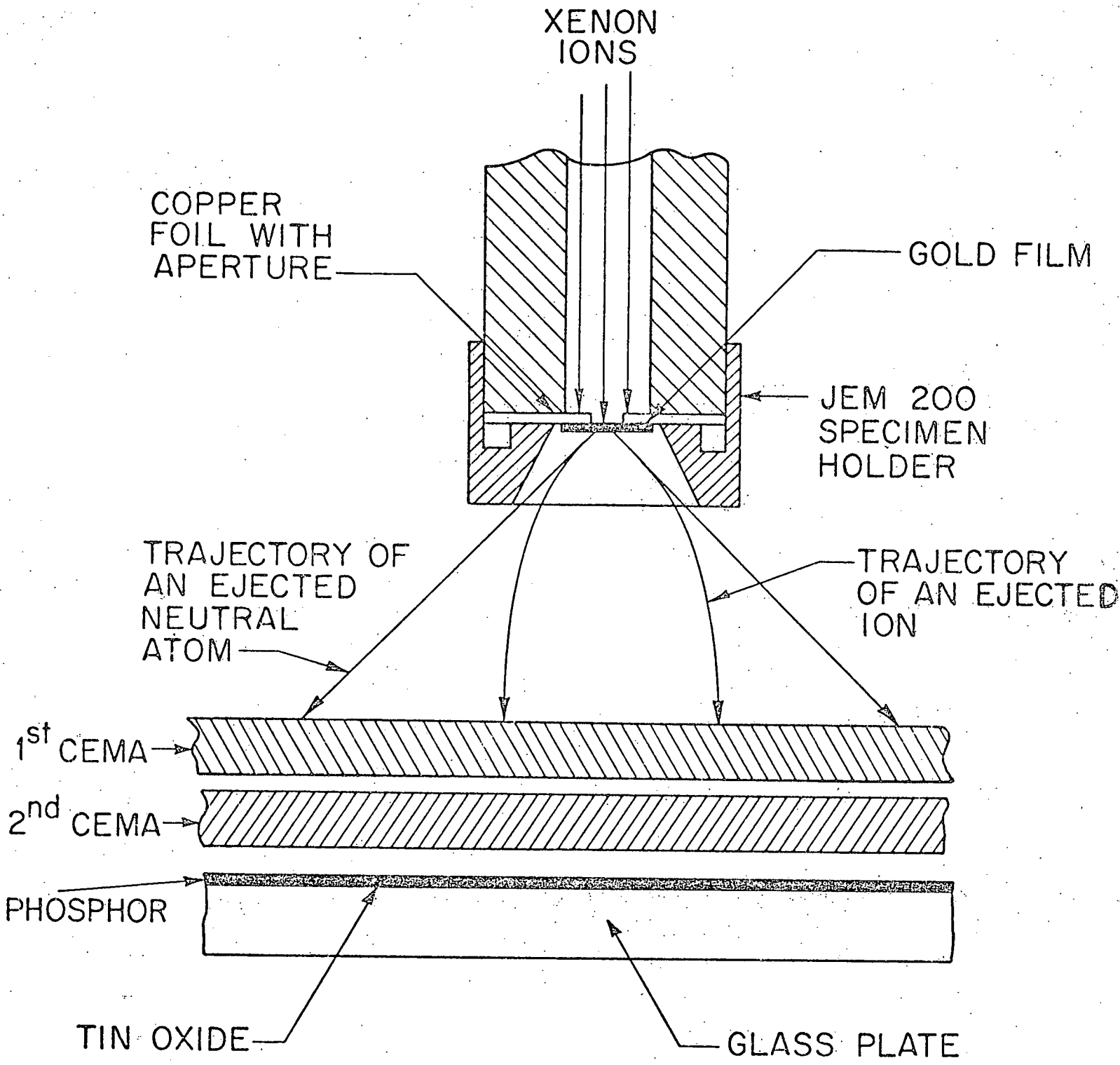
XENON IONS
COPPER FOIL WITH APERTURE
GOLD FILM
JEM 200 SPECIMEN HOLDER
TRAJECTORY OF AN EJECTED NEUTRAL ATOM
TRAJECTORY OF AN EJECTED ION
1st CEMA
2nd CEMA
PHOSPHOR
TIN OXIDE
GLASS PLATE

Fig. 1

Figure 2. Experimental apparatus for the study of focused collision sequences showing the ion gun, magnetic beam analyzer, specimen holder and CEMA detector.

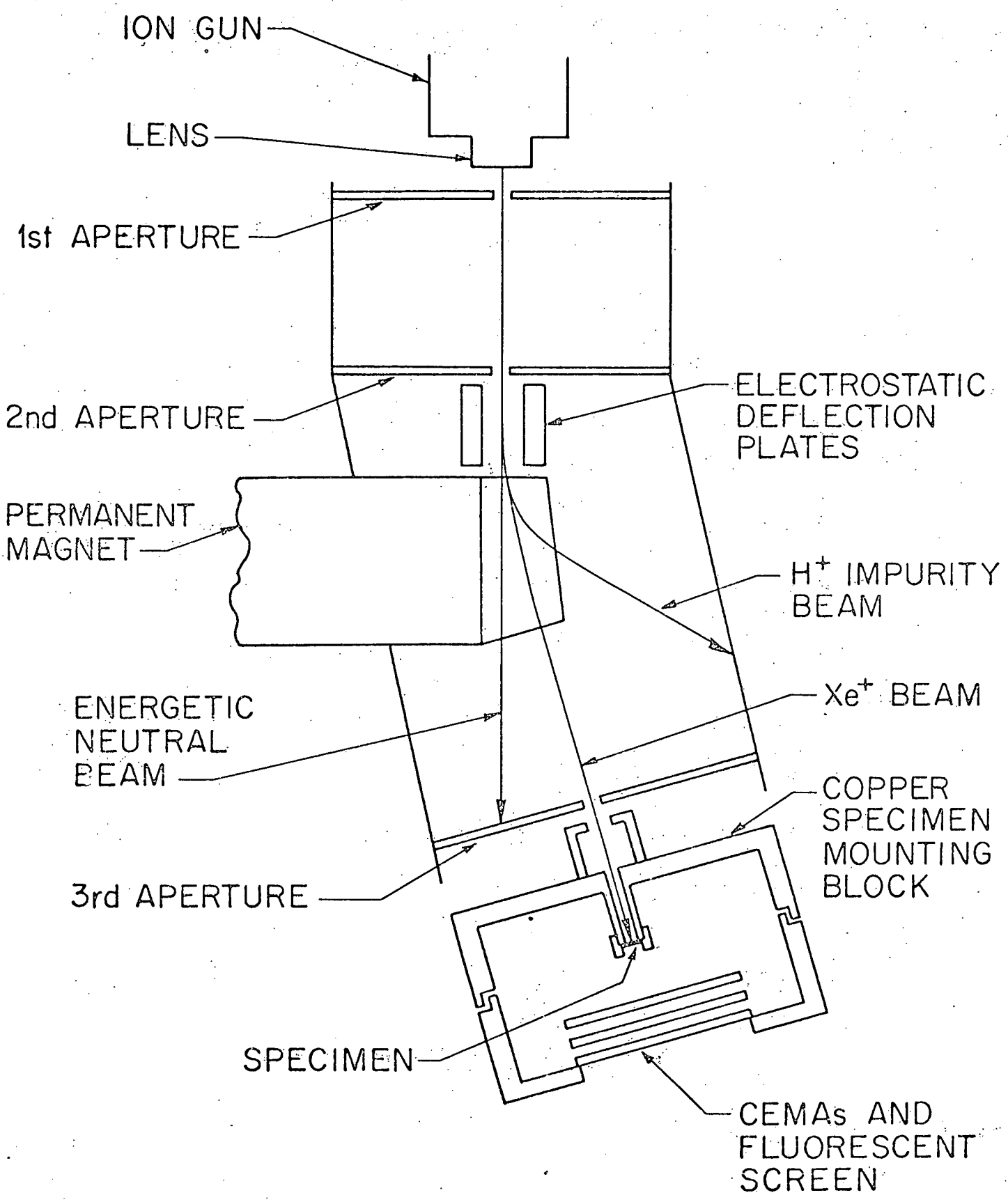
ION GUN
LENS
1st APERTURE
2nd APERTURE
ELECTROSTATIC DEFLECTION PLATES
PERMANENT MAGNET
H+ IMPURITY BEAM
Xe+ BEAM
ENERGETIC NEUTRAL BEAM
COPPER SPECIMEN MOUNTING BLOCK
3rd APERTURE
SPECIMEN
CEMAs AND FLUORESCENT SCREEN

Fig. 2

Figure 3. A schematic diagram of the electronic system used to measure the Xe^+ ion current and the CEMA detector output.

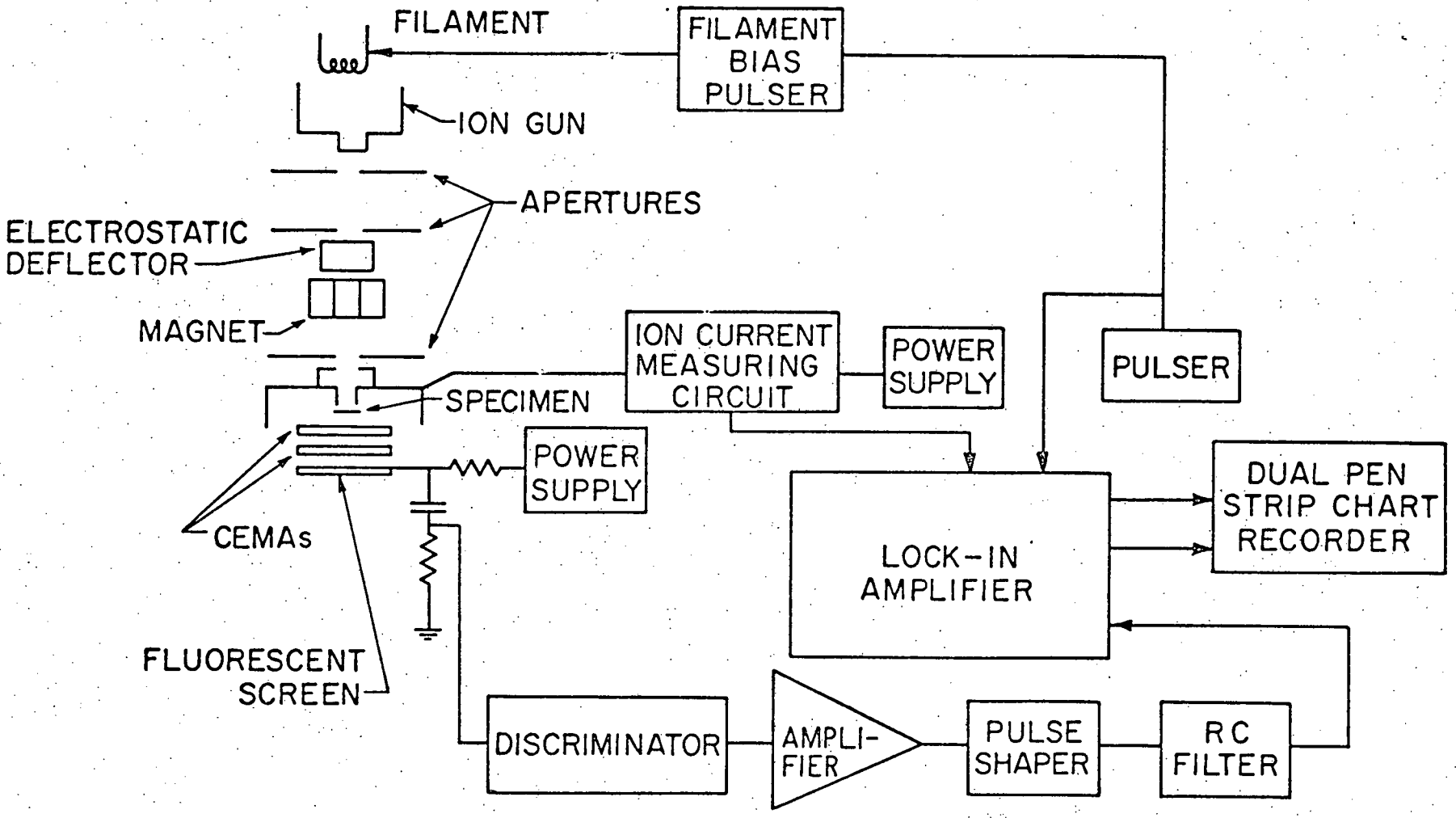
FILAMENT
FILAMENT BIAS PULSER
ION GUN
APERTURES
ELECTROSTATIC DEFLECTOR
MAGNET
ION CURRENT MEASURING CIRCUIT
POWER SUPPLY
PULSER
SPECIMEN
POWER SUPPLY
CEMAs
DUAL PEN STRIP CHART RECORDER
LOCK-IN AMPLIFIER
FLUORESCENT SCREEN
DISCRIMINATOR
AMPLI-FIER
PULSE SHAPER
RC FILTER

Fig. 3

By calibration, the ratio R can be converted directly into a transmission sputtering yield S, where

$$S = \frac{\text{number of transmission sputtered particles detected}}{\text{number of ions striking the specimen}} .$$

Despite the fact that the irradiated areas are small ($\lesssim 8 \times 10^{-5} cm^2$), and the ion current density is low ($\lesssim 6.5 \times 10^{12}$ ion $cm^{-2} sec^{-1}$), this system (CEMAs and electronics) is capable of measuring transmission sputtering yields as low as 1×10^{-9}. This is lower by a factor of $\sim 10^6$ than other transmission sputtering experiments (2).

The physical quantities actually observed in these experiments are the transmission sputtering yield and the ion current as a function of time. This is easily converted to a transmission sputtering yield as a function of ion dose. Using published data on the sputtering rate for Xe^+ on Au (4), this in turn can be converted into transmission sputtering yield as a function of the change in foil thickness.

The initial specimen thickness (before irradiation) is determined using transmission electron microscopy (TEM) by measuring the projected width of microtwins which lie on (111) planes. Due to problems of carbon contamination in the electron microscope, these measurements are not made on the specimens which are actually used for transmission sputtering experiments, but rather on a nearby portion of the same as-deposited specimen. This leads to some uncertainty in the initial thickness of the irradiated specimens; 20% variations in a given as-deposited specimen are typical.

2. Experimental results and discussion

Transmission sputtering experiments have been performed at 120K, with both 700eV and 300eV Xe^+ ions. The 700eV experiments fall into two categories; (1) low dose and (2) high dose. In the low dose experiments specimens of various initial thicknesses (140 to 280A) are irradiated to ion doses of $\sim$(4 to 8)$\times 10^{15}$ ion cm^{-2}, which sputter-thin the specimens by $\sim$25 to 50A. During this experiment the transmission sputtering yield is measured as a function of time. The specimens are then removed and the entire irradiated area is inspected for holes using TEM at a magnification of 30,000 to 50,000X; this is done to eliminate the possibility that the output is due to the Xe^+ ion beam passing through microscopic holes. Results for four such experiments are shown in Fig. 4.

Figure 4. Transmission sputtering yield versus foil thickness for four low dose experiments at 700eV.

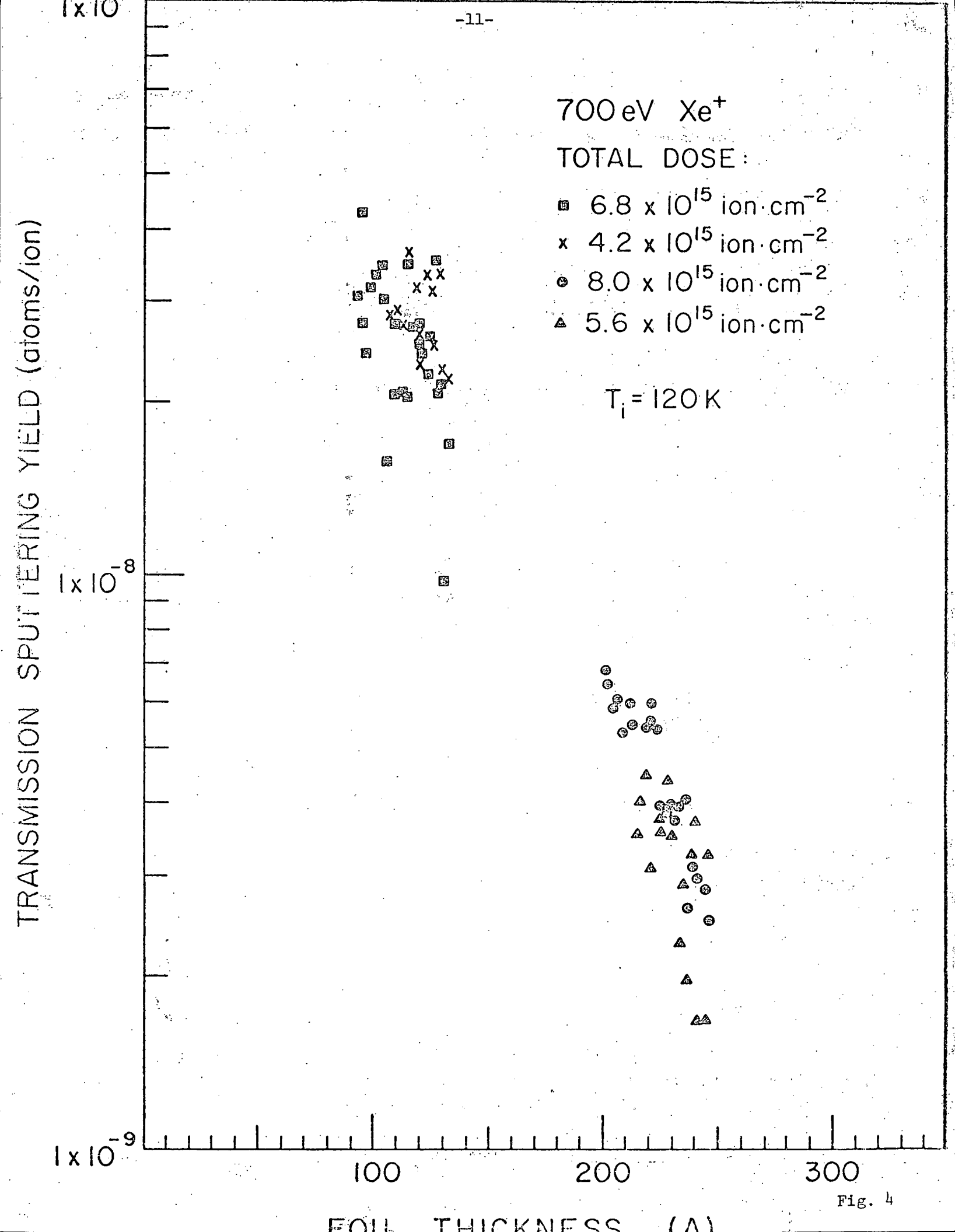
700 eV Xe+
TOTAL DOSE:
6.8 x 10^15 ion·cm^-2
4.2 x 10^15 ion·cm^-2
8.0 x 10^15 ion·cm^-2
5.6 x 10^15 ion·cm^-2
T_i = 120 K
TRANSMISSION SPUTTERING YIELD (atoms/ion)
1x10
1x10^-8
1x10^-9
100
200
300
FOIL THICKNESS (A)

Fig. 4

We note first that there is a consistent rise in the transmission sputtering yield as the specimen thickness decreases, and that the measured transmission sputtering yields for specimens of similar thickness are quite reproducible. A record notable feature is that the measured transmission sputtering yields are quite small ($<10^{-7}$ atoms/ion). We must be cautious in interpreting this in terms of the number of FCS which reach the bottom surface of the foil, for two reasons. First, we are dependent upon an unspecified surface process to cause ejection of an unspecified particle (gold atom or ion, adsorbed impurity atom or ion) which is detected by the CEMA; we do not know the probability of this ejection event. Second, since the transmission sputtered species is unknown, we do not know the sensitivity of the CEMA to it. Indeed, an overall detection efficiency of unity for all FCS reaching the bottom foil surface would be surprising; what we can say is that the number of FCS reaching the bottom surface of the specimen is greater than or equal to the measured number.

Since these results are reproducible, the uncertainty in absolute numbers does not prevent us from determining the range of these events. To obtain a clearer picture of this, in which the uncertainty in initial specimen thickness plays a smaller role, high dose experiments are used. In this case the foils are irradiated until sputter thinning causes them to rupture. In Fig. 5 this point is easily identified by the sharp rise in output due to the Xe^+ going through the hole(s) in the specimen to the CEMAs. Post-irradiation TEM inspection of these specimens always revealed holes.

For initially thinner specimens the results are similar (Fig. 6). In both cases there is an exponential dependence of the transmission sputtering yield on foil thickness, with comparable slope in the semi-log plots. Due to the uncertainty in initial foil thickness, the apparent difference in foil thickness at the point where rupture occurs cannot be consifered significant. However, the larger transmission sputtering yield at the point of rupture for the initially thinner specimen of Fig. 6, which has been irradiated with a lower ion dose, proves to be a consistent feature.

To test the possibility that the observed output is due to channeling, high dose experiments have been performed using 300eV Xe^+. If the observed output is due to channeling then changes in the ion energy should have a dramatic effect on the output, while for FCS, much smaller changes are expected. The results in Fig. 7 show that the behavior at 300eV is essentially similar to that at 700eV in Figs. 4 and 5. The major difference between the two experiments is that the

Figure 5. Transmission sputtering yield versus foil thickness for a high dose experiment at 700eV.

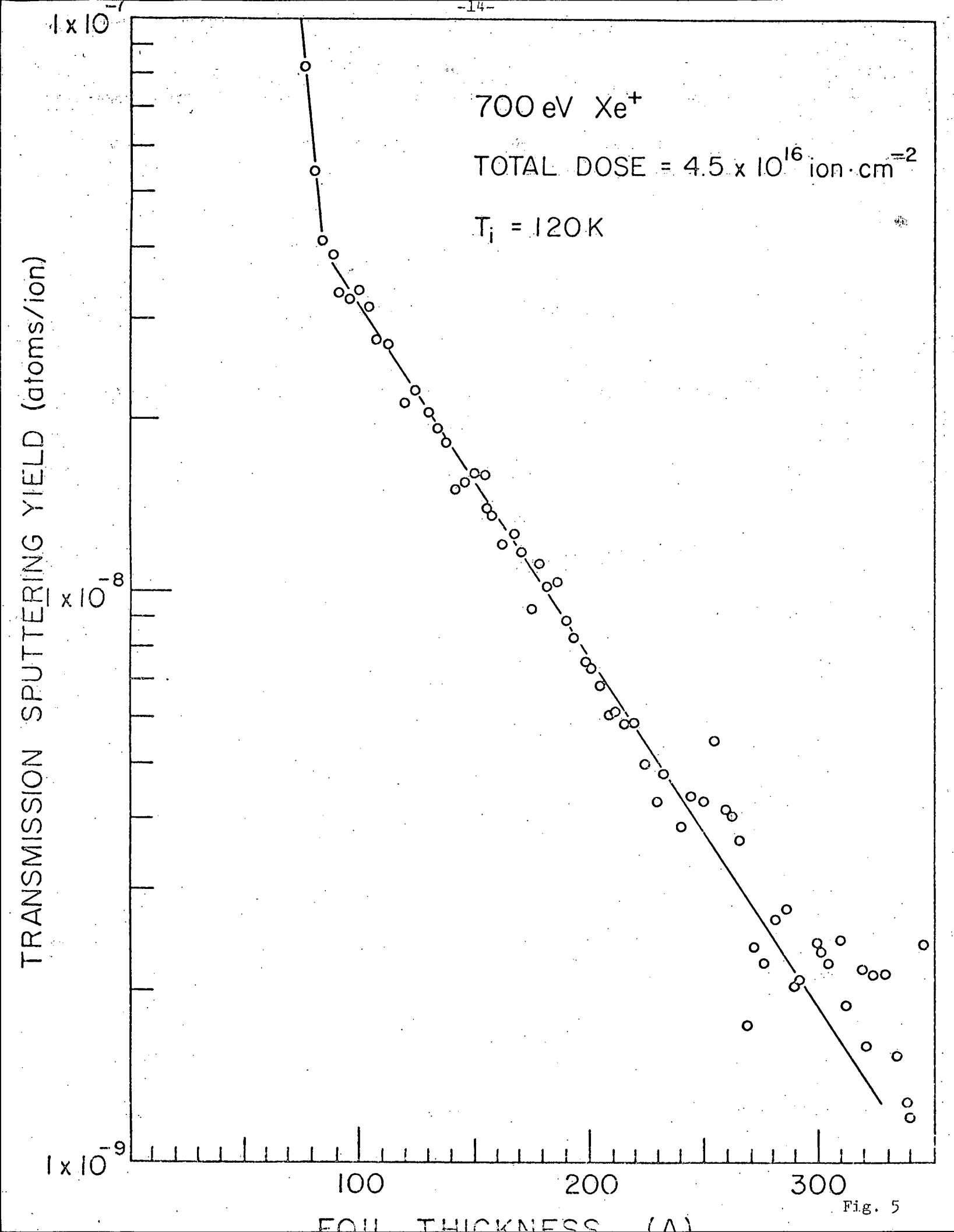
700 eV Xe+
TOTAL DOSE = 4.5 x 10^16 ion·cm^-2
Ti = 120K
TRANSMISSION SPUTTERING YIELD (atoms/ion)
1 x 10^-7
1 x 10^-8
1 x 10^-9
100
200
300
FOIL THICKNESS (A)

Fig. 5

Figure 6. Transmission sputtering yield versus foil thickness for a high dose experiment at 700eV.

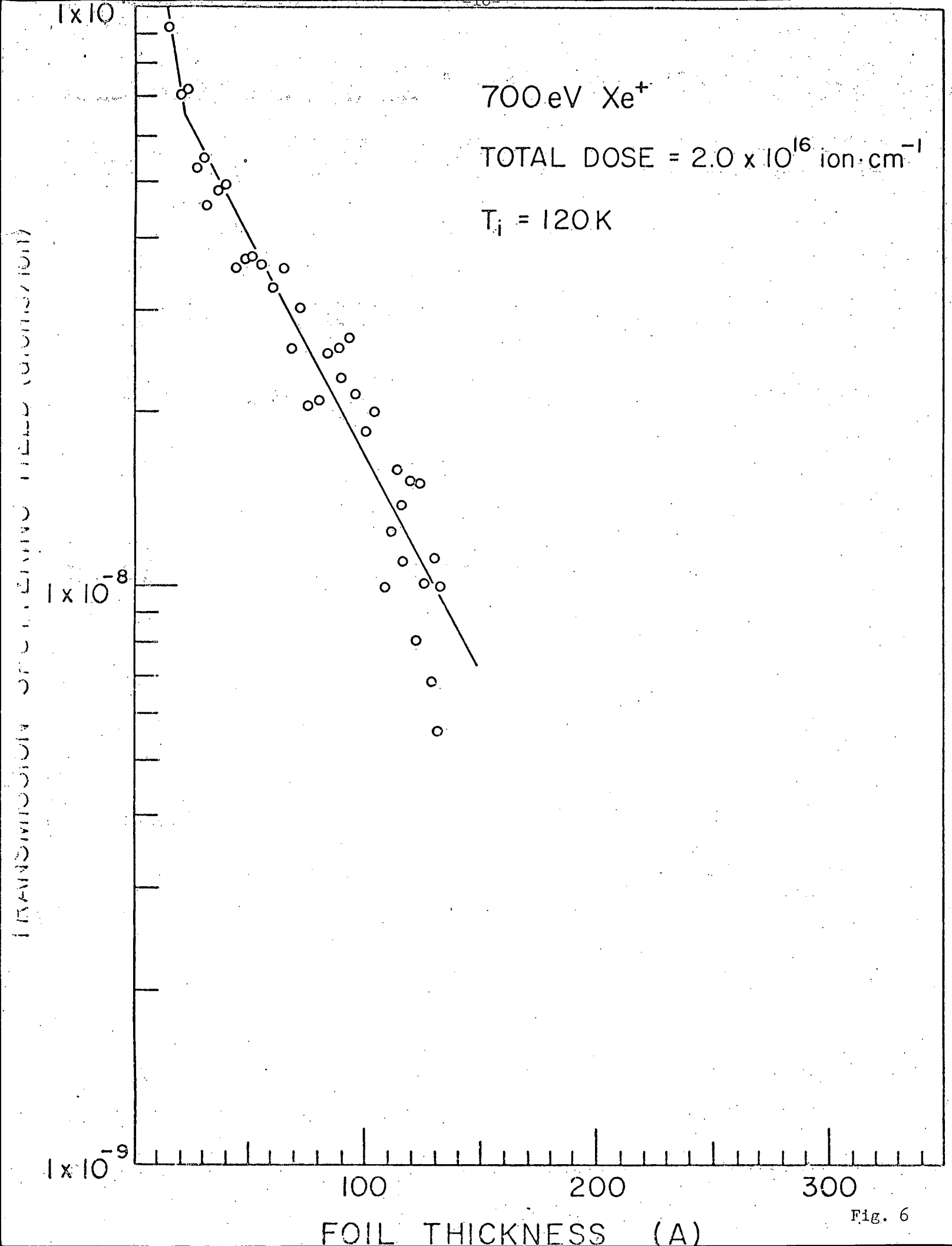
700 eV Xe+
TOTAL DOSE = 2.0 x 10^16 ion·cm^-1
T_i = 120 K
1 x 10
1 x 10^-8
1 x 10^-9
100
200
300
FOIL THICKNESS (A)

Fig. 6

Figure 7. Transmission sputtering yield versus foil thickness for a high dose experiment at 300eV.

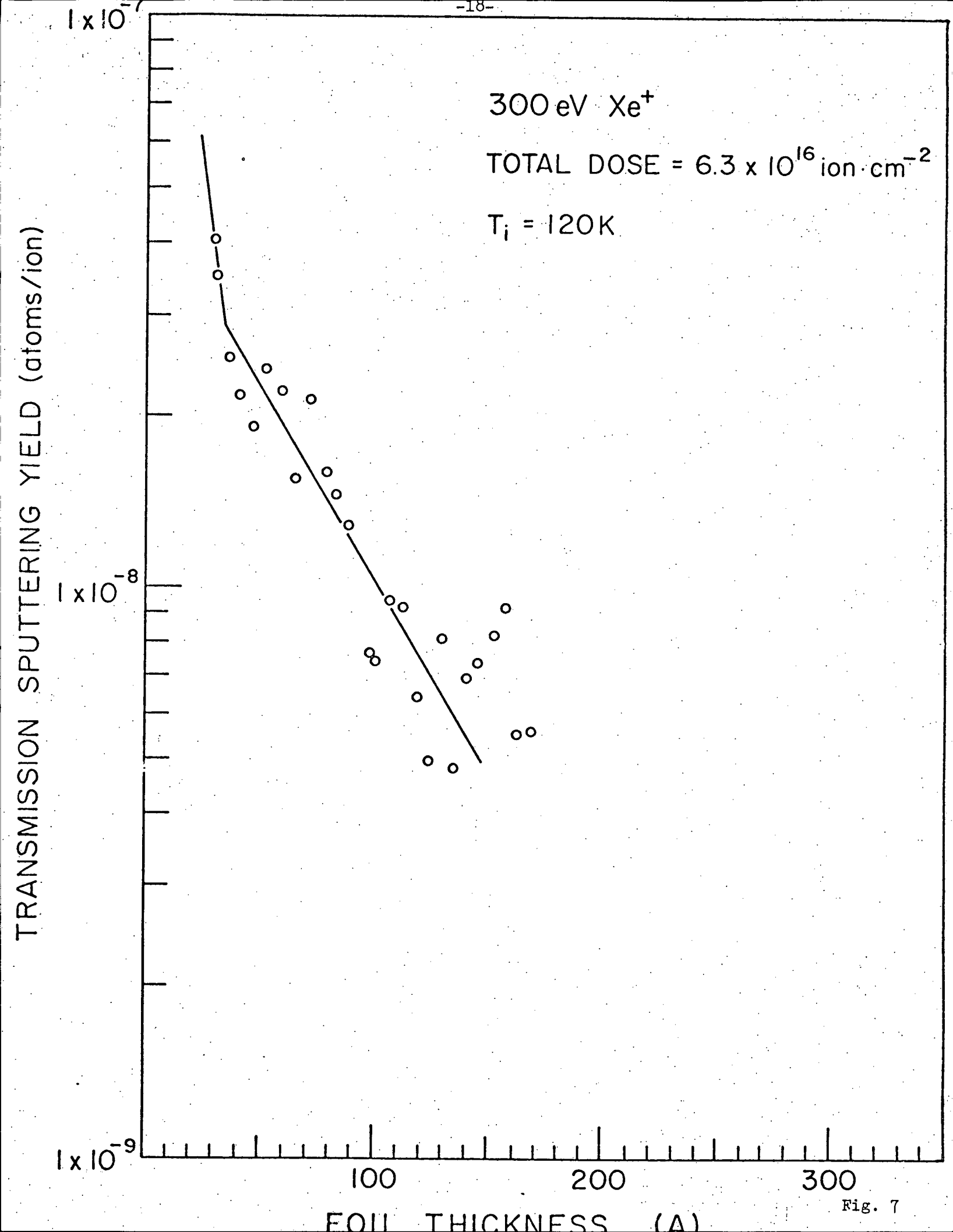
300 eV Xe+
TOTAL DOSE = 6.3 x 10^16 ion·cm^-2
Ti = 120K
TRANSMISSION SPUTTERING YIELD (atoms/ion)
1 x 10^-7
1 x 10^-8
1 x 10^-9
100
200
300
FOIL THICKNESS (A)

Fig. 7

transmission sputtering yield at the point of rupture is lower than for the 700eV experiments. However, it should be noted that due to the lower sputtering rate for 300eV Xe^+, a higher ion dose is necessary to achieve the rupture of a given specimen than at 700eV. If we plot the transmission sputtering yield at the point of rupture versus total ion dose for both 300eV and 700eV (see Fig. 8) we see that there is a definite correlation; for larger ion doses, the maximum yield is smaller. The origin of this effect is unclear at present, but it does assist in demonstrating that the results at 700eV and 300eV are in good accord, effectively eliminating the possibility that the observed output is due to channeling.

B. Atom-Probe Field-Ion Microscope Studies (A. Wagner and Dr. J. Amano)

1. Technical improvements in the atom-probe FIM

a. Automated photographic system

An automated photographic system which is essentially identical to the design described in Scanlan et al. (5) has been constructed for use with the atom-probe. The system consists of an Automax ciné camera equipped with a 1000 foot film chamber, a high voltage pulser and associated control electronics. This system is being used to perform isochronal annealing experiments and controlled pulsed-field evaporation experiments on tungsten which had been irradiated with low-energy helium ions (see Section 3).

b. Modified ion gun

The ion gun described previously (6,7) has been modified so that the plasma chamber and lens elements may be floated above ground potential. This design permits irradiations to be performed with the FIM specimen held at ground potential and thus avoids the problem of field-emission induced melting and failure of the FIM specimen (see Fig. 9).

In operating the ion gun, a gas such as H_2, He, Ne, Ar or Xe is continuously bled through a stainless steel cylindrical plasma chamber held at a positive potential. The gas is ionized in the plasma chamber by a magnetically confined 2 mA beam of 30 to 100eV electrons emitted from a heated tungsten filament. The ions produced in the plasma chamber are extracted, accelerated and focused onto the FIM specimen which is held at ground potential. The kinetic energy of the ions is simply equal to the plasma chamber potential. The ion gun can produce a 4 cm diameter beam of 200 to 3000eV gas ions at current densities of 0.01 to 10μA cm^{-2} with gas pressures of $3 \cdot 10^{-6}$ to $5 \cdot 10^{-4}$ Torr respectively.

Figure 8. Maximum transmission sputtering yield at the point of foil rupture versus total Xe^+ ion dose.

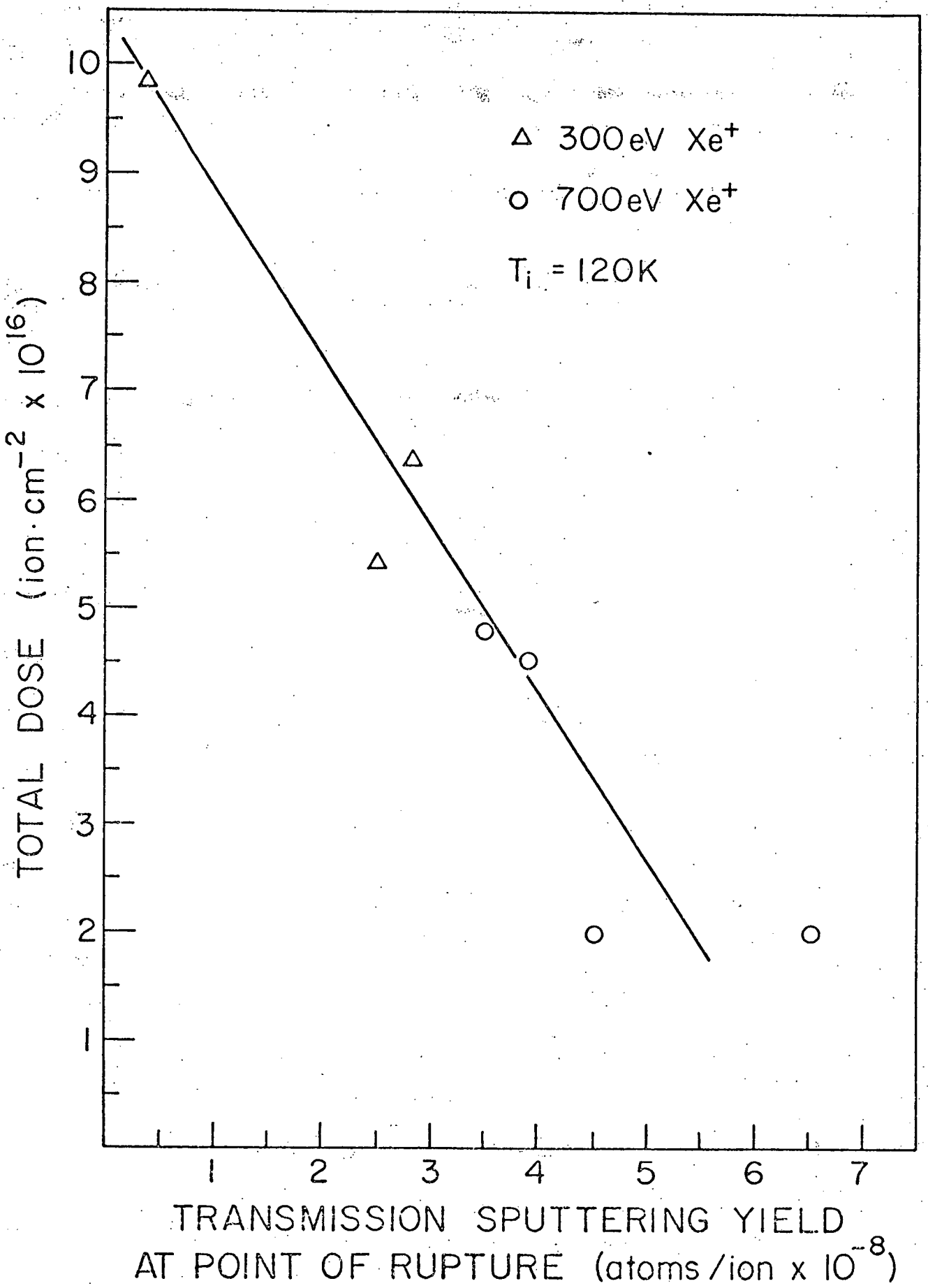
△ 300eV Xe+
○ 700eV Xe+
Ti = 120K
TOTAL DOSE (ion·cm-2 x 10^16)
10
9
8
7
6
5
4
3
2
1
1
2
3
4
5
6
7
TRANSMISSION SPUTTERING YIELD
AT POINT OF RUPTURE (atoms/ion x 10^-8)

Fig. 8

Figure 9. A schematic diagram of the low energy gas ion gun which is used for irradiating FIM specimens in situ. The extractor and accelerating electrodes are held at fixed fractions (0.92 and 0.80 respectively) of the plasma chamber potential (V_p). The kinetic energy of the ions striking the grounded FIM specimen is equal to V_p.

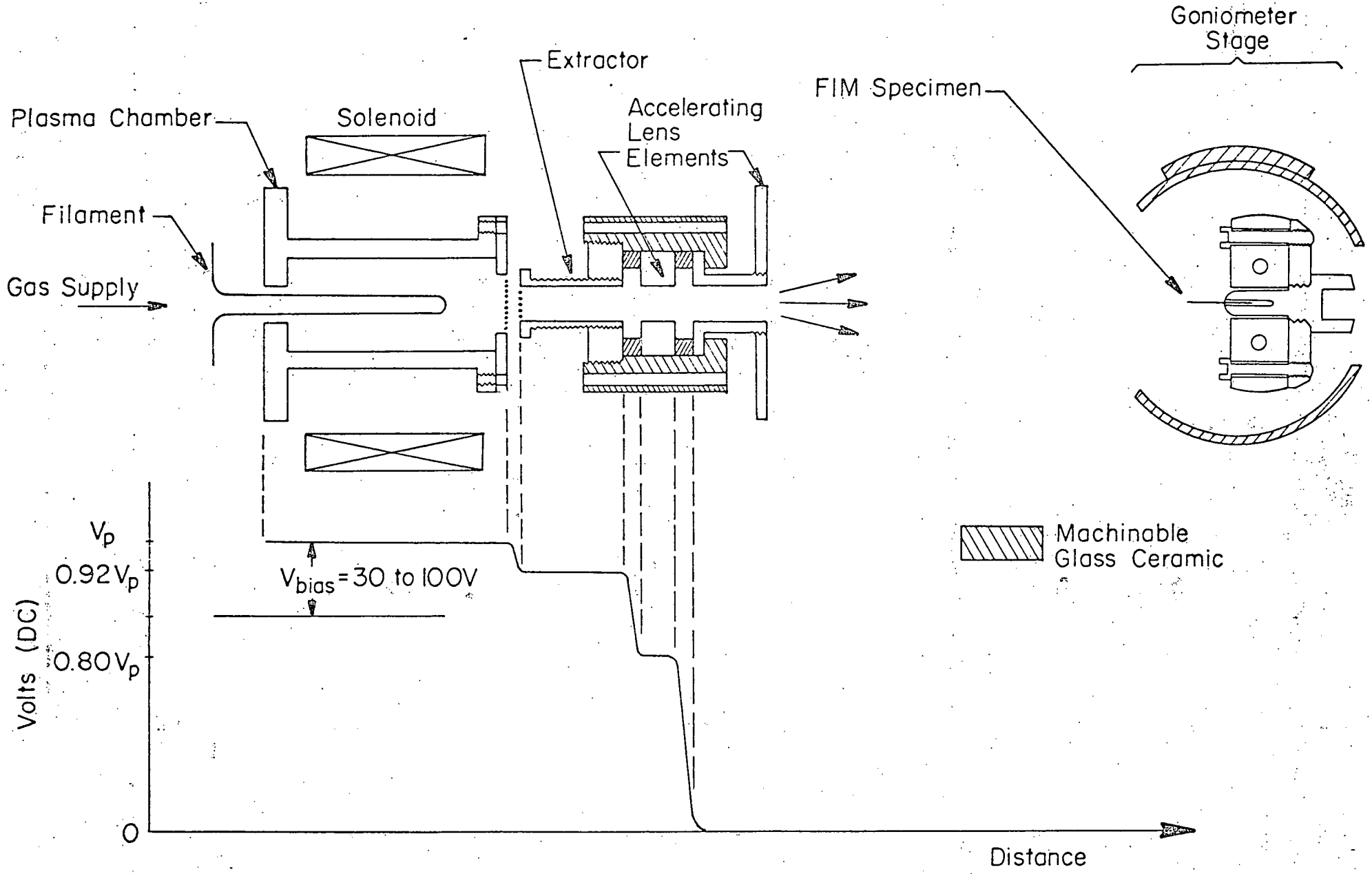
Goniometer Stage
Extractor
FIM Specimen
Plasma Chamber
Solenoid
Accelerating Lens Elements
Filament
Gas Supply
V_p
$0.92V_p$
$0.80V_p$
V_{bias} = 30 to 100V
Volts (DC)
0
Distance
Machinable Glass Ceramic

Fig. 9

This ion gun is presently being used to inject low energy (~300eV) helium atoms into tungsten (see Section 3).

2. Spatial distribution of atomic species in alloys

In this section we present results on three alloy systems which show the spatial distribution of the alloying elements in the unirradiated materials. The specific aims of the research program are: (1) the measurement of the size distribution, number density and composition of the irradiation induced precipitates in neutron-irradiated W(Re) alloys, (2) the determination of the extent of irradiation induced segregation of titanium and zirconium to voids and irradiation induced resolution of titanium-zirconium carbides in neutron-irradiated TZM, (3) the determination of irradiation induced segregation to the free surface of the FIM tip in low-energy ion-irradiated stainless steels.

The objective in all three experiments is to try to understand the data obtained in terms of possible implications on the mechanism(s) responsible for the suppression or enhancement of void formation. An effort is also being made to determine the role played by gaseous impurities (e.g. He) in the nucleation and stabilization of voids (see Sections 3 and 4).

The results in the following sections show the spatial distribution of alloying elements in unirradiated materials through the use of a composition profile. Before discussing these results we will describe the physical principle behind the composition profile illustrated in Fig. 10. Fig. 10(a) shows an FIM tip formed from a binary alloy of B (solute) in A (solvent). The tip contains a single precipitate which is rich in B; the solute atoms are denoted by the solid black circles. The magnification is adjusted so that during the course of pulsed field-evaporation of the specimen all the atoms (A and B) contained within a cylindrical volume element are chemically analyzed by the atom probe. Fig. 10(b) shows the corresponding composition profile; the number of B atoms versus the cumulative number of A plus B atoms. The cumulative number of atoms is proportional to depth (z), since the specimen is chemically analyzed by dissecting atomic planes sequentially; in a typical experiment the specimen is analyzed to a depth of ~250A. If the B atoms are distributed uniformly† the average slope of the plot in the regions away from the indicated precipitate determines the average composition of the alloy. In the region of the precipitate the average slope of the composition profile yields the

† We will use the term uniform to indicate an absence of any gross segregation effects in the volume of space sampled.

Figure 10. During the course of an atom-by-atom disection of an FIM specimen by the pulsed field-evaporation technique, the atom probe determines the distribution of chemical species in an approximately cylindrical volume element of the specimen as shown in 10(a). A plot of the number of B atoms (we consider here the case of a binary alloy consisting of A and B atoms) as a function of the total number of atoms (A plus B) detected yields a composition profile. The presence of a local composition variation produced by a precipitate results in a change of slope of the composition profile; this is illustrated in 10(b).

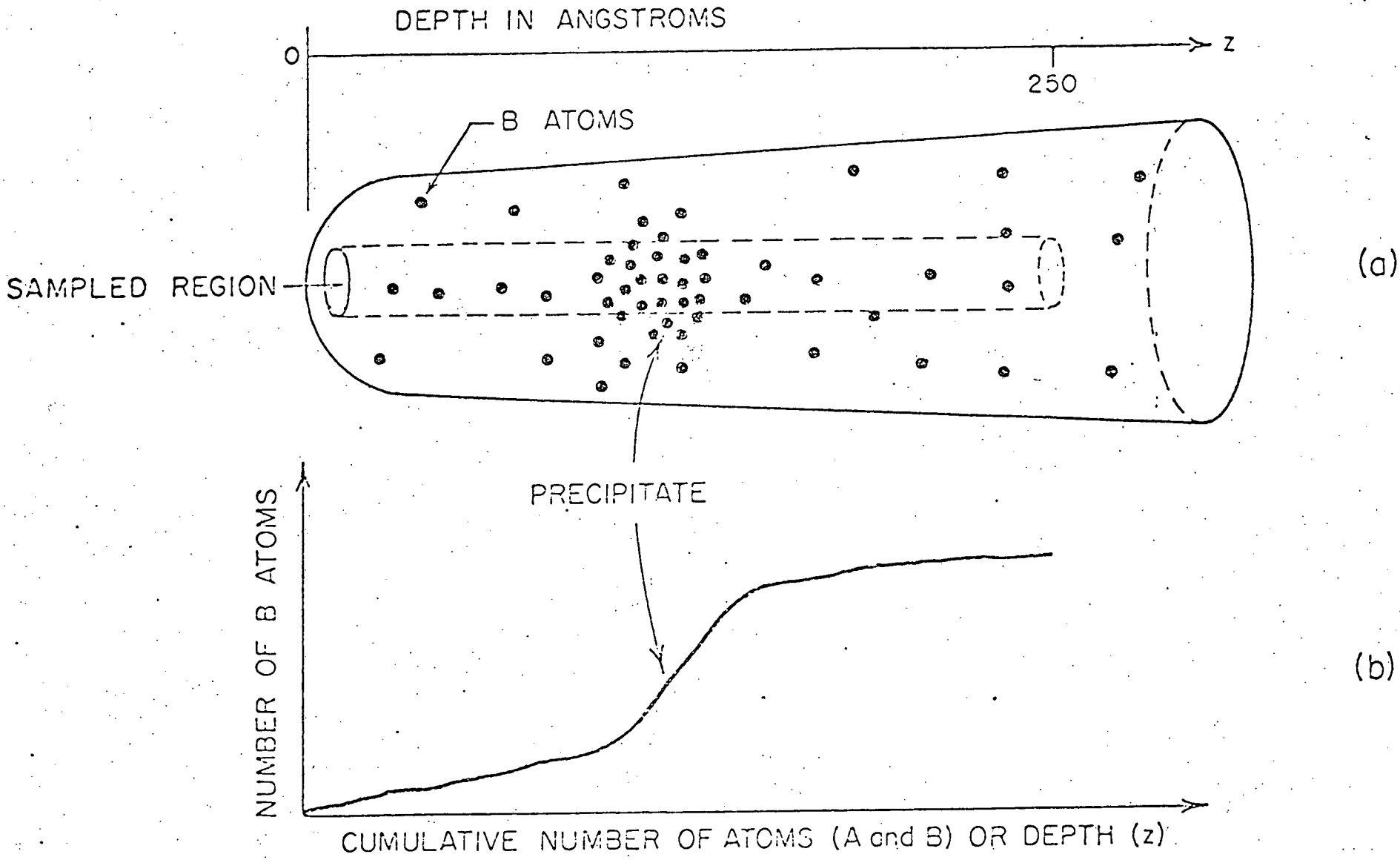
DEPTH IN ANGSTROMS
0
z
250
B ATOMS
SAMPLED REGION
(a)
PRECIPITATE
NUMBER OF B ATOMS
CUMULATIVE NUMBER OF ATOMS (A and B) OR DEPTH (z)
(b)

Fig. 10

precipitate's average composition. The identification of this change in composition as being caused by a precipitate can be confirmed from the microstructural information present in the FIM image. It is also possible to use the composition profiles, in conjunction with the FIM images, to distinguish among: (1) clustering, (2) short-range order (or anti-clustering), (3) composition fluctuations, and (4) pre-precipitation clusters such as Guinier-Preston zones. In this section we use the term cluster to indicate any local composition fluctuation which is obviously greater than the composition fluctuations expected in a random solid solution.

a. Tungsten (Rhenium) system

The addition of Re to W strongly suppresses swelling (void formation) in fast neutron irradiated W(Re) alloys (8). It is our objective to determine how the Re is redistributed as a result of the fast neutron irradiation treatment and to study the irradiation produced precipitates in this alloy.

An FIM specimen was prepared from off-the-spool W-25 at.% Re thermocouple wire; its (m/n) spectrum has been previously published [Hall et al. (7)]. Figure 11 shows the composition profiles for the two stable Re isotopes (^{185}Re and ^{187}Re). This experiment demonstrated that the Re isotopes can be distinguished from the immediately adjacent W isotopes (^{184}W and ^{186}W). The average composition of the rhenium determined for the ^{185}Re isotope was 10.6 at.% and for the ^{187}Re isotope it was 14.8 at.%; hence, the overall composition was 25.4 at.% Re as determined from the average slopes of the profiles shown in Fig. 11. The rhenium concentration was also found by a least-squares analysis of the atom-probe data to be 22 ± 2 at.% which agrees with the nominal concentration of 25 at.%. The first conclusion drawn from this experiment was that a Re concentration of 25 at.% or higher could be easily detected in tungsten. A second conclusion is that the vast majority of the Re atoms were in solid solution in this specimen; this conclusion was based on the fact that the measured Re concentration was approximately equal to the nominal composition of the alloy and also that the FIM image showed no evidence for precipitation. A third conclusion is that there was no evidence for any pre-precipitation. A fourth conclusion is that the composition profiles exhibit composition fluctuations about the average Re isotope compositions. To date we have been unable to conclude whether or not there is any evidence for short-range order (anti-clustering) obtainable from the composition profiles. These results on W and W/25% Re will serve as controls for future work on fast-neutron irradiated samples.

Figure 11. Composition profiles of $^{185}Re^{+3}$ (61.6 to 61.9 amu) and $^{187}Re^{+3}$ (62.3 to 62.6 amu) in a W-25 at.% Re alloy. The average composition obtained from these plots are 10.6 at.% ^{185}Re and 14.8 at.% ^{187}Re for a total Re concentration of 25.4 at.% as determined from the average slopes. A least-squares fit to the (m/n) histogram which takes into account the overlapping tails caused by energy deficits yields an average Re composition of 22 ± 2 at.% which agrees with the nominal composition.

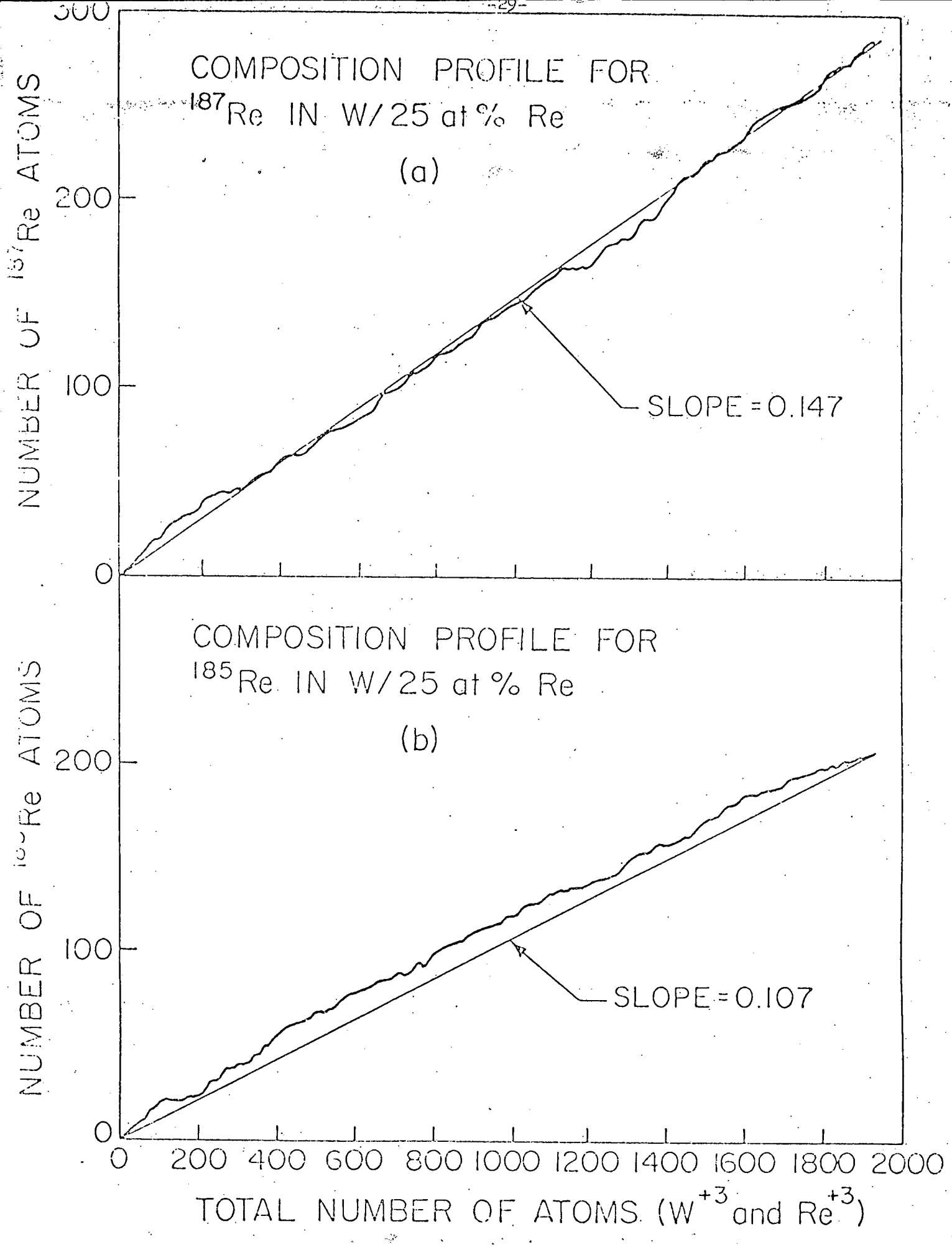
COMPOSITION PROFILE FOR
^{187}Re IN W/25 at % Re
(a)
SLOPE = 0.147
NUMBER OF ^{187}Re ATOMS
COMPOSITION PROFILE FOR
^{185}Re IN W/25 at % Re
(b)
SLOPE = 0.107
NUMBER OF ^{185}Re ATOMS
0
100
200
300
0 200 400 600 800 1000 1200 1400 1600 1800 2000
TOTAL NUMBER OF ATOMS (W^{+3} and Re^{+3})

Fig. 11

b. Molybdenum (titanium + zirconium) system

Both Mo/1.0 at.% Ti and Mo/1.0 at.% Ti/0.08 at.% Zr (TZM) exhibit an enhanced swelling behavior when compared to molybdenum specimens irradiated under identical conditions to the same fast neutron dose (8,9). At present we are engaged in a study to determine the role(s) played by the Ti in Mo/1.0 at.% Ti and the Ti and Zr in TZM in causing this swelling enhancement. It is interesting to note, by contrast, that Johnston et al. (10) have found Ti and Zr additions to be effective swelling inhibitors in a series of model Fe/Cr/Ni alloys.

The concentration of Ti was found to be 0.28 at.% in the Mo/1.0 at.% Ti alloy and 0.26 at.% in the TZM alloy. The measured concentrations of titanium are approximately 1/4 of the nominal concentration in both materials. There are two possible explanations for this discrepancy: (1) an undetermined amount of titanium may field evaporate in the +2 charge state and hence would be superimposed on the Mo^{+4} portion of the spectrum; or (2) the remaining titanium may go undetected because it is not in solid solution, i.e., the remaining Ti may be tied up in the form of TiC precipitates which exist at a number density that is below the limit of detection of the FIM. In support of the second explanation the work of Chang and Perlmutter (11) has shown that Mo_2C, TiC and ZrC precipitates can form in both Mo(Ti) and TZM. In addition, our own limited observations of FIM tips by transmission electron microscopy have shown the appearance of precipitates in both the Mo/1.0 at.% Ti and the TZM wire used in this study.

The composition profiles of Ti and Zr in TZM are shown in Fig. 12; each step in the ordinate scale corresponds to single Ti or Zr atom. The Ti atoms observed were distributed uniformly throughout the specimen; from the slope of the composition profile the Ti concentration is 0.26 at.%. The Ti distribution in the Mo/1.0 at.% Ti alloy was similar. All of the Zr atoms detected were contained in a single cluster; this Zr cluster was detected just before the FIM tip failed and it may have contributed to the failure of the tip. The measured Zr concentration was 0.13 at.% compared to the normal 0.08 at.%. The probability of this Zr cluster being found in a random solid solution was calculated to be $<10^{-6}$, hence we may safely conclude that this represents a non-random fluctuation in the Zr concentration which indicates a positive binding enthalpy between Zr atoms in TZM. We would also like to point out that neither the Ti nor the Zr was associated with carbon and therefore the observed Zr cluster is not due to a small carbide precipitate.

Figure 12. Composition profiles for Ti and Zr in TZM. The Ti appears to be uniformly distributed in the material whereas the Zr is concentrated in a single cluster.

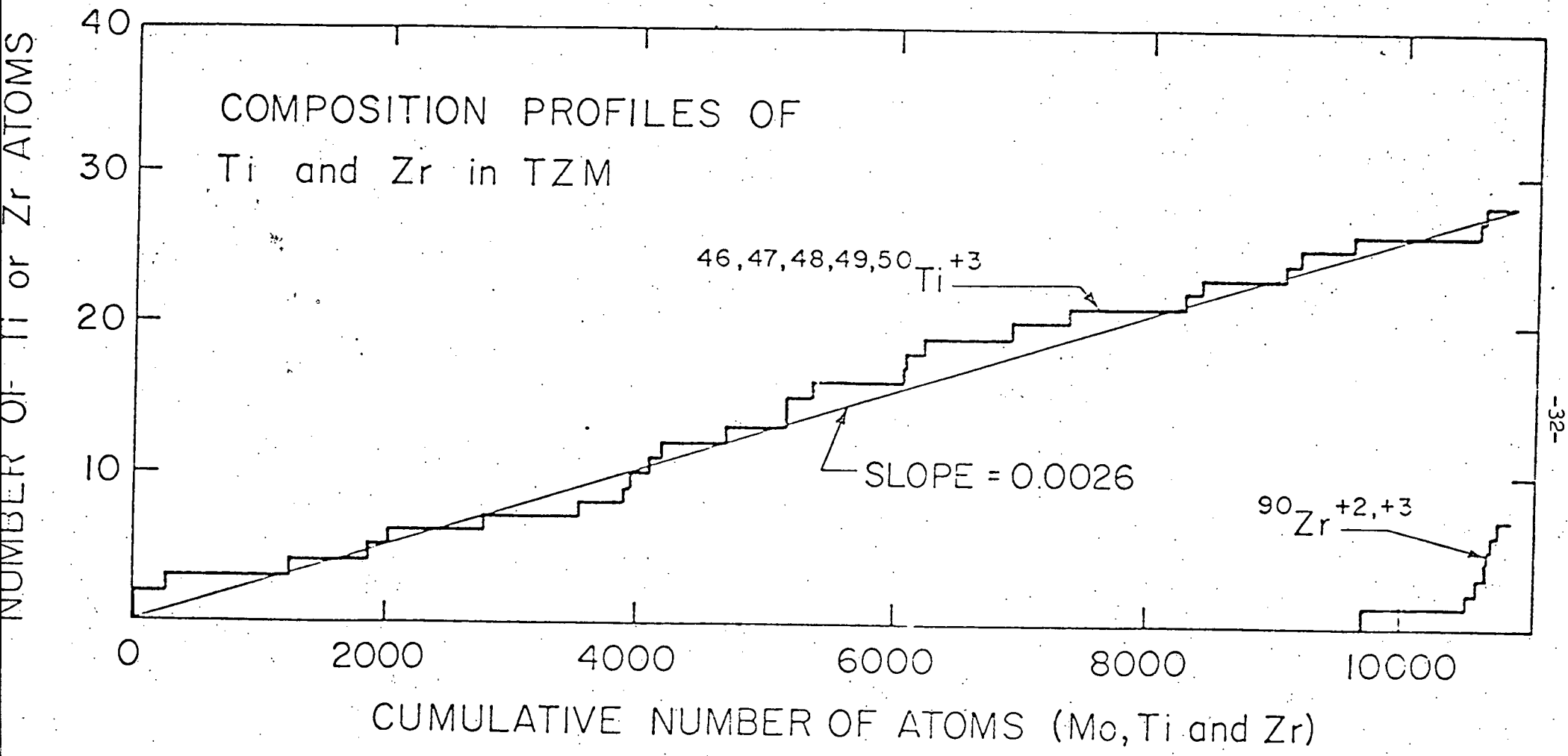
COMPOSITION PROFILES OF
Ti and Zr in TZM
46,47,48,49,50 Ti +3
SLOPE = 0.0026
90 Zr +2,+3
NUMBER OF Ti or Zr ATOMS
CUMULATIVE NUMBER OF ATOMS (Mo, Ti and Zr)
0
2000
4000
6000
8000
10000
10
20
30
40

Fig. 12

A comparison of the present results with the results on the irradiated specimens should allow us to comment in detail on the changes produced in the spatial distribution of Ti and Zr atoms in the alloy as a result of the fast neutron irradiations. Furthermore, any changes in the measured concentration of Ti and Zr in solid solution due to the neutron irradiation should allow us to comment on the possibility of re-solution of the Ti-Zr carbide precipitates.

c. Low swelling stainless steel (LSIA)

A low swelling stainless steel alloy (LSIA) developed at the Oak Ridge National Laboratory (ORNL) by Bloom et al. (12) has been analyzed. To date we have restricted our work to unirradiated specimens of this alloy because of the high radioactivity of the neutron irradiated specimens. The alloy LSIA contains 2.06 at.% Si and 0.16 at.% Ti as swelling inhibitors. It is the purpose of the present study to determine the role played by these swelling inhibitors.

All the alloying elements (Fe, Cr, Ni, Mn, Mo, C, Si and Ti) in LSIA were readily identified and the concentrations measured by the atom probe technique are in good agreement with the chemical composition as supplied to us by ORNL as shown in Table 1. In addition, an analysis of the spatial distribution of each alloying element revealed the existence of a cluster which was rich in the minor alloying additions (Si, Ti, C, Mo, Mn) and poor in the major components (Fe, Ni, Cr) as shown in Table 1. The probability of this cluster forming in a random alloy was calculated to be $<10^{-11}$, hence this cluster indicates a positive binding enthalpy between the minor alloying additions. It is possible that clusters such as the one described are responsible for the observed enhanced reduction in swelling when both Si and Ti are added to stainless steel [Johnston et al. (10)].

d. Neutron-irradiated alloys

Techniques for producing wire shaped specimens from bulk neutron irradiated materials (e.g. tensile specimens) have been developed. These techniques have been successfully applied to neutron irradiated Mo (1.0 at.% Ti) and with somewhat less success to neutron irradiated TZM. Unfortunately, thus far we have not been successful in obtaining FIM images of the Mo (1.0 at.% Ti) specimens which we have processed into wire form. At this time we have not attempted to produce FIM specimens from either the irradiated TZM or the irradiated W-Re alloys.

We presently have two sets of wire alloys being irradiated in EBR-II* and

* One set of specimens is being handled by Dr. J. J. Laidler of Hanford Engineering and Development Laboratory and the second set by Dr. M. Grossbeck of the Metals and Ceramics Division of the Oak Ridge National Laboratory.

Table 1. Comparison of the composition of a low swelling stainless steel (LS1A) as determined by chemical analysis and by atom probe FIM analysis for the bulk specimen and for a non-random cluster.

Element	Chemical analysis (Atomic %)	Atom probe analysis of the bulk specimen (Atomic %)†	Atom probe analysis of a cluster (Number of Atoms)
Fe	64.0	62.2 ± 1.1	1
Cr	17.4	14.5 ± 0.5	0
Ni	12.9	16.2 ± 0.6	3
Mn	2.0	2.6 ± 0.2	1
Mo	1.0	1.8 ± 0.2	2
C	0.37	0.4 ± 0.1	2
Si	2.1	1.7 ± 0.2	3
Ti	0.16	0.20 ± 0.06	2
Other	0.15	0.5 ± 0.1	0
Totals	100.1	100.1	14

† The uncertainties were calculated from the $\sqrt{N}/\Sigma N$ values where N is the number of atoms counted.

anticipate a much higher probability of success with these specimens since: (1) they are in wire form and do not require processing from bulk form; and (2) they will increase our present supply of potential FIM specimens by over a factor of ten.

3. The range and mobility of helium in tungsten

The interaction of low energy (<10keV) light ions (e.g. He) with materials is an area of increasing concern with regard to materials problems in the fusion reactor program. In addition, the nucleation and stabilization of voids in fast neutron irradiated materials is believed to be strongly affected by the presence of helium produced within the material as a result of (n,α) nuclear reactions.

The objective of our experiment is to directly measure the range of low-energy He ions and the migration energy of interstitial He atoms in tungsten.

a. Description of the experiment

A tungsten FIM specimen is irradiated in-situ with 300eV He^+ ions at approximately normal incidence to the <110> direction as indicated in Fig. 9. With an energy of only 300eV a He^+ ion can transfer a maximum of only ∿25eV to a tungsten atom. Since the displacement energy in tungsten is ∿44eV (13), no self-interstitial atoms or vacancies should be created in the bulk.* If the specimen temperature is low enough to prevent migration of the injected helium, then the state of the specimen just after irradiation will consist of interstitial helium deposited in a perfect tungsten lattice with a depth distribution determined solely by the range profile of the 300eV He^+ ions. The specimen is then chemically analyzed using the atom-probe FIM technique and a composition profile (see Section 2 for a description of a composition profile) for the helium is plotted as shown in Fig. 13. This composition profile yields the range profile of the helium as discussed in the next section. Furthermore, the temperature at which the helium interstitials become mobile can be determined by irradiating at a series of temperatures. If the specimen temperature is above the temperature at which helium interstitials become mobile, then the helium injected during the irradiation will diffuse out to the free surface of the FIM tip, and thus we expect to see a sharp decrease in the helium concentration as the irradiation temperature is increased. By determining the temperature at which the helium becomes mobile an approximate value of the migration energy can be made. In principle, by measuring the total dose of helium and then comparing it to the measured amount of helium detected in the specimen, the fraction of helium reflected from the tungsten specimen can also be determined.

---

* Sputtering of the surface may occur since the energy required to produce a surface vacancy is much lower than the displacement energy and, in fact, our FIM images do indicate surface disordering following irradiation with 300eV He^+.

Figure 13. Composition profiles showing the spatial distribution of helium in in tungsten. Profiles 1 and 3 are for tungsten irradiated with 300eV He^+ ions at 48K along the <110> direction. Profiles 2 and 4 are for unirradiated samples and constitute controls. The helium interstitials are not mobile at 48K.

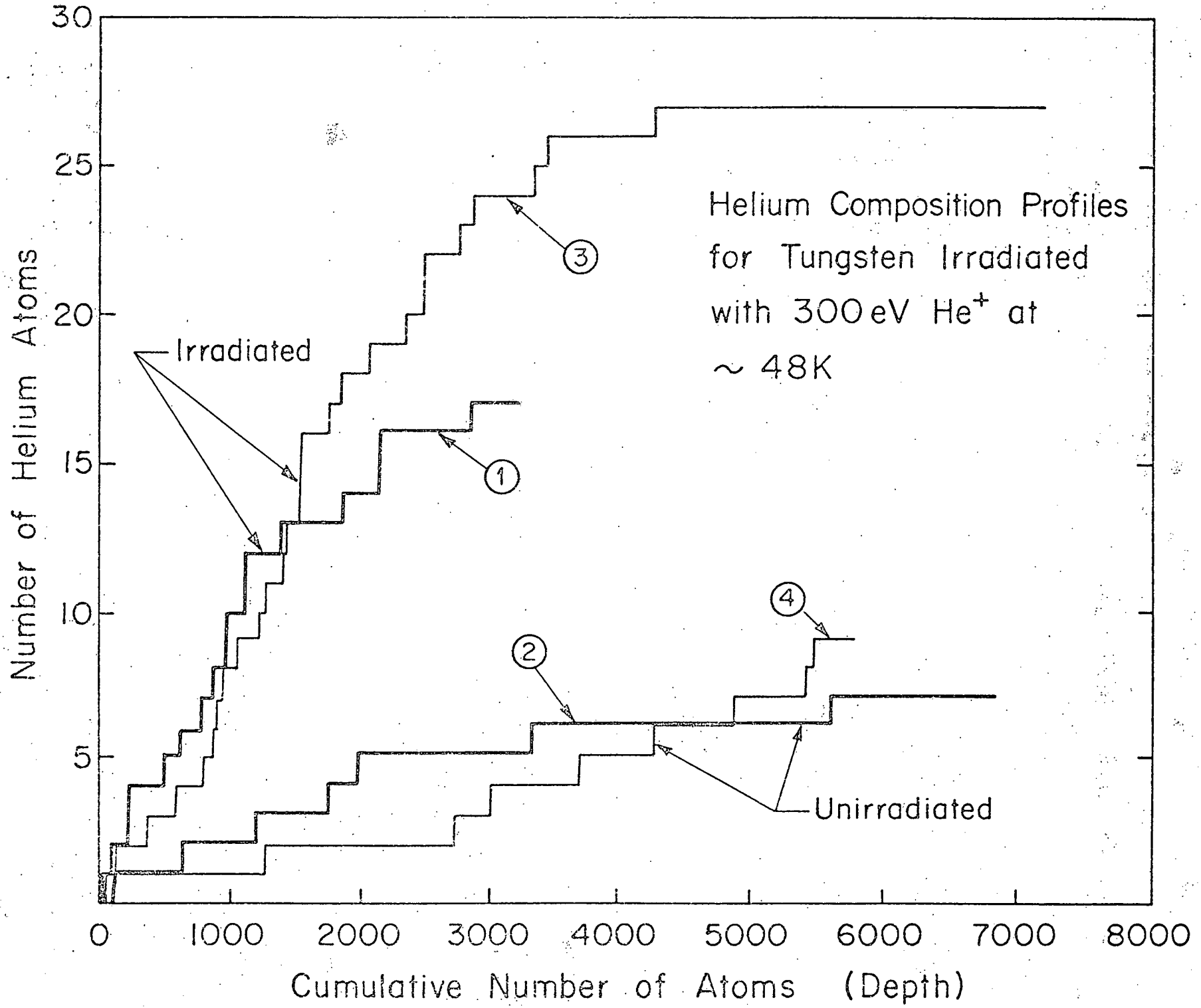
Helium Composition Profiles
for Tungsten Irradiated
with 300 eV He^+ at
~ 48K
Irradiated
Unirradiated
1
2
3
4
Number of Helium Atoms
Cumulative Number of Atoms (Depth)
0
1000
2000
3000
4000
5000
6000
7000
8000
5
10
15
20
25
30

Fig. 13

b. Results

In Fig. 13 we show two helium composition profiles (labeled 1 and 3) for a tungsten specimen irradiated with 300eV helium ions to a dose of $\sim 3 \times 10^{15}$ ion cm^{-2} along the <110> direction at 48K. Also shown in this figure are two helium profiles (labeled 2 and 4) for unirradiated specimens which serve as controls. All four runs were performed on the same specimen in the sequence indicated by the labeling of the profiles; i.e., 1 was first, 2 second, etc. Between each run the specimen was annealed to ~373K for several hours. Controls 2 and 4 were performed under the same conditions as irradiations 1 and 3 except that the tip was shielded from the ion beam in control 2 while in control 4 the specimen was held at a positive potential of 450 Vdc and thus only neutral helium atoms from the ion gun could hit the specimen. A number of conclusions can be drawn from this experiment:

(1) From the difference in the slopes of the helium profiles of the irradiated versus the unirradiated tungsten, we can conclude that at 48K helium is being retained in the lattice after irradiation.*

(2) The sigmoidal shape of profile 3 indicating a rise and then a fall in the helium concentration with distance is consistent with a range profile for the helium ions. This result suggests that particle range measurements are possible and also that at 48K the interstitially deposited helium is <u>not</u> mobile. At this time we have not been able to assign a distance scale to the horizontal axis in Fig. 13 since we have not yet determined the absolute number of atoms on the surface that were within the area analyzed by the atom probe. Thus, we are not yet able to report on either the range or the reflection coefficient of 300eV helium on tungsten at this time.

(3) The absence of a statistically significant difference between controls 2 and 4 indicates that our measurements are <u>not</u> affected by a neutral component of helium in the ion beam.

In addition to the helium atoms and tungsten substrate hydrogen, carbon and oxygen were also detected. In Figs. 14, 15 and 16 we show the hydrogen, carbon and oxygen composition profiles for the runs shown in Fig. 13. These profiles indicate

* The presence of helium in the control experiments is due to the random arrival of helium atoms from the gas phase. The number of helium events in the controls could be reduced by as much as a factor of ten through the use of a differentially pumped ion-gun.

Figures 14, 15 and 16. Composition profiles for hydrogen, carbon and oxygen for the runs shown in Fig. 13. The only species detected other than tungsten and helium are hydrogen, carbon and oxygen. The profiles show that they are only present in the near surface region and thus trapping of the helium interstitials at impurities can be ruled out.

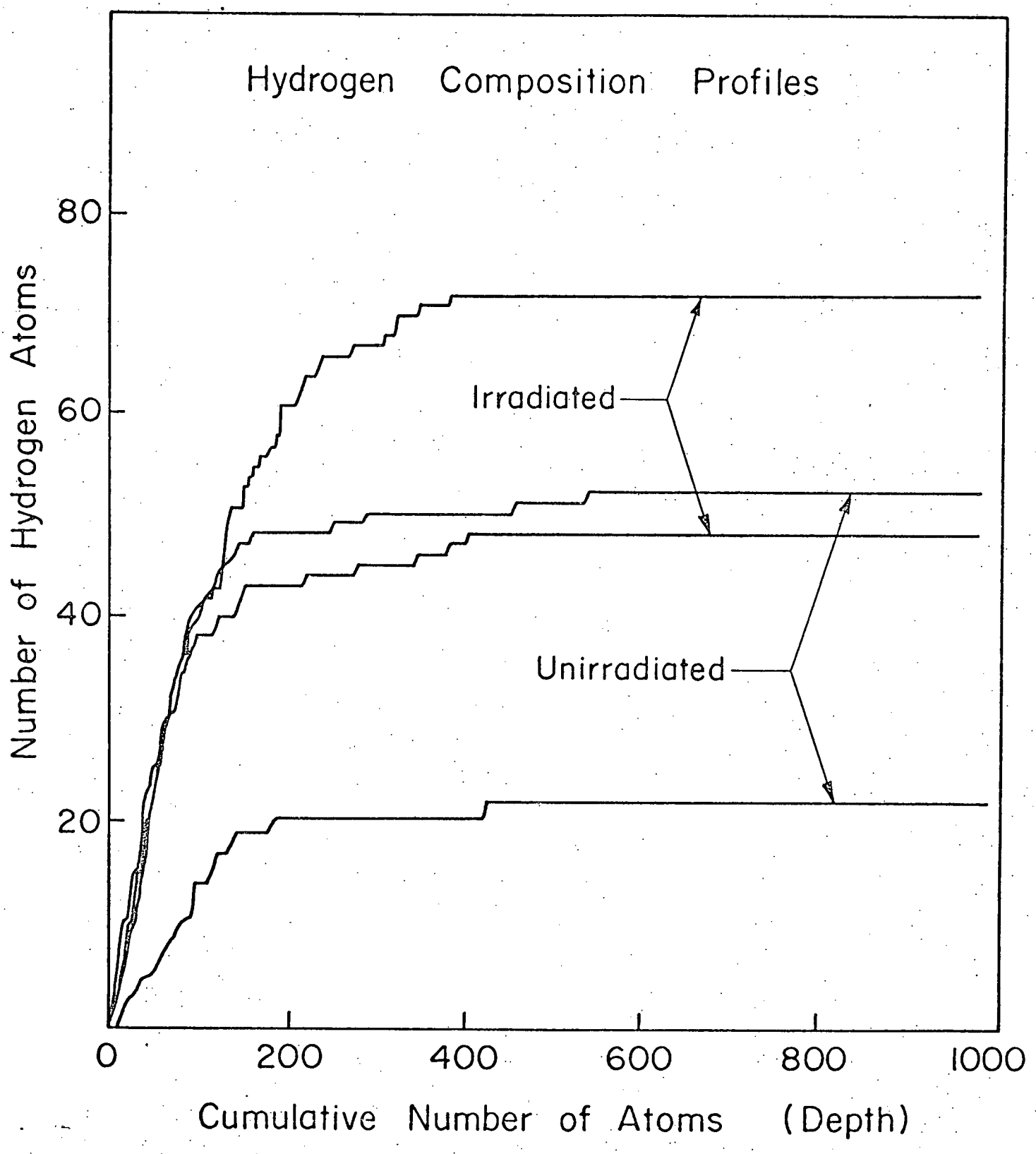
Hydrogen Composition Profiles
Number of Hydrogen Atoms
80
60
40
20
Irradiated
Unirradiated
0
200
400
600
800
1000
Cumulative Number of Atoms (Depth)

Fig. 14

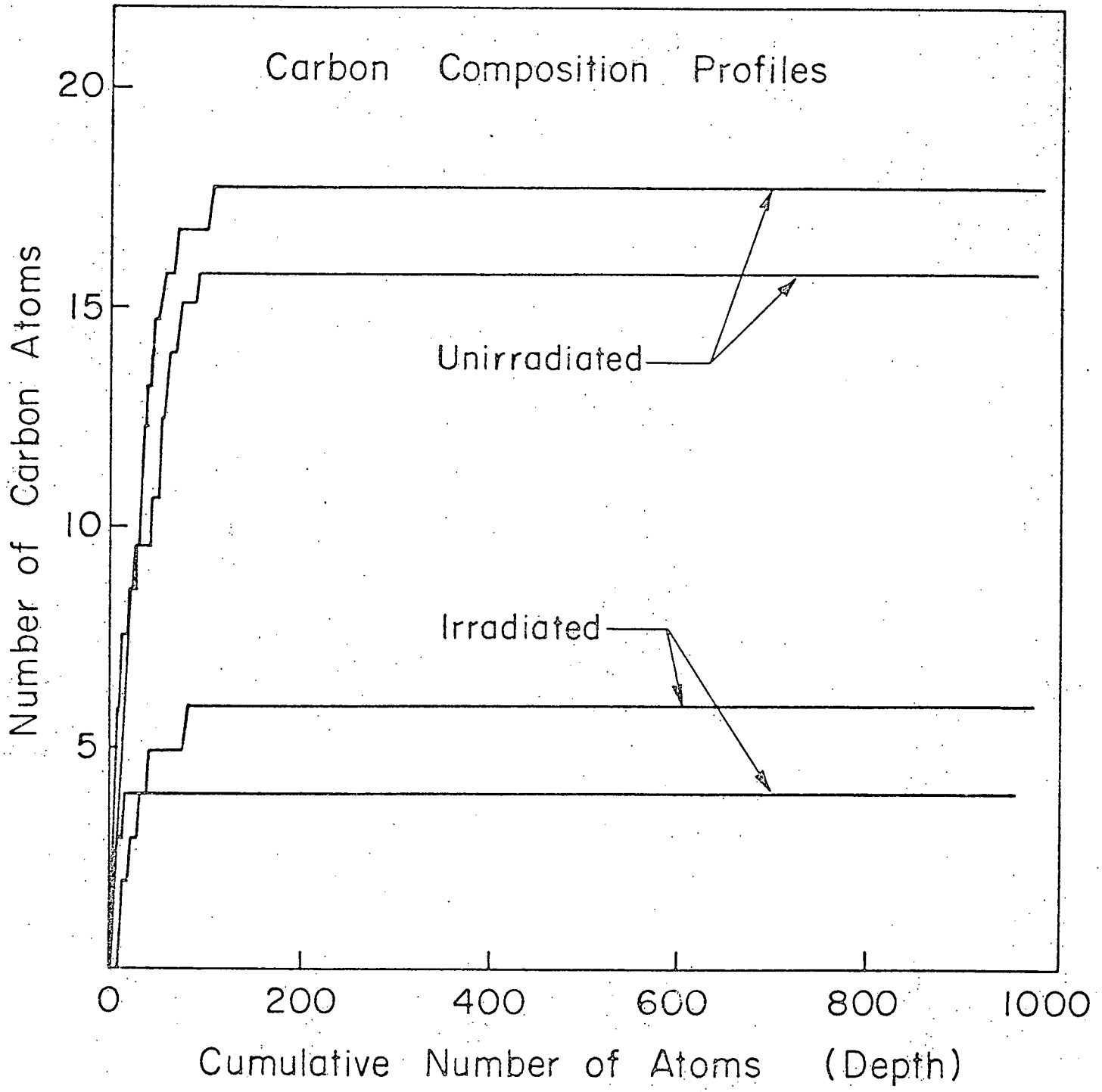
Carbon Composition Profiles
Number of Carbon Atoms
20
15
10
5
Unirradiated
Irradiated
0
200
400
600
800
1000
Cumulative Number of Atoms (Depth)

Fig. 15

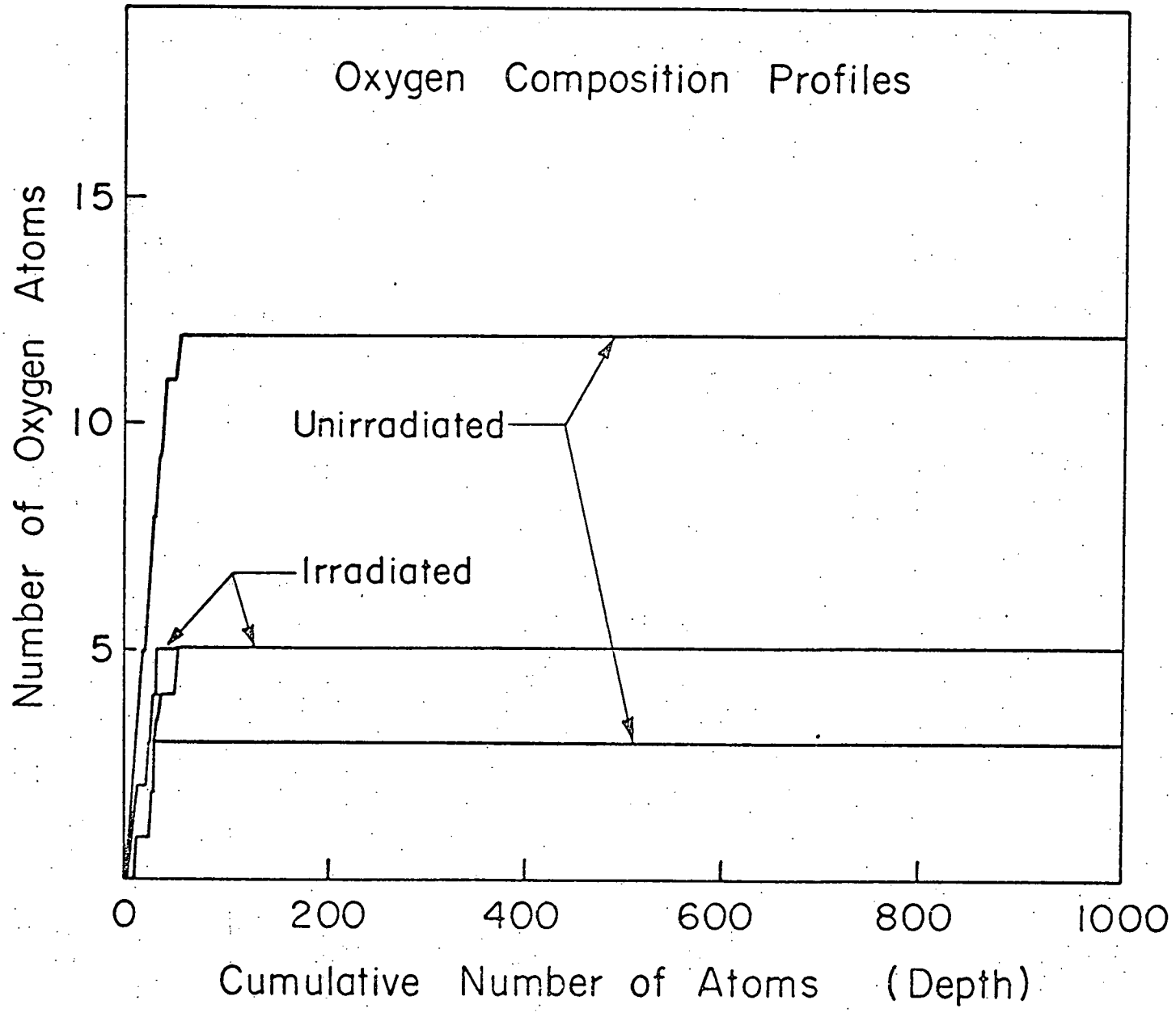
Oxygen Composition Profiles
Number of Oxygen Atoms
15
10
5
Unirradiated
Irradiated
0
200
400
600
800
1000
Cumulative Number of Atoms (Depth)

Fig. 16

that beyond roughly the first 600 atoms, only W and He are present in the lattice. This result is important since it allows us to conclude that the helium atoms are not trapped at impurities. The most probable origin of the hydrogen, carbon and oxygen atoms is from residual gases in the FIM; these gases are adsorbed on the surface of the specimen during the irradiation and during the ∿2 hours required to pump out the helium after an irradiation. This explanation is supported by the observation that just prior to the atom probe analysis the vapor gaseous components in the vacuum system are H_2(7.8×10^{-10}torr), He(0.5×10^{-10}torr), CO(0.7×10^{-10}torr) and CH_4(0.05×10^{-10}torr). During the atom probe analysis the high electric field prevents the H_2, CO and CH_4 from reaching the FIM tip.

In order to rule out the probability of helium atoms being trapped at vacancies or self-interstitial atoms created by the 300eV helium irradiation, an isochronal recovery experiment was performed. In this experiment a tungsten specimen was irradiated along the <110> direction with 300eV He^+ ions at 30K. After the irradiation approximately two (110) planes corresponding to ∿4A of material were field evaporated from the specimen. The procedure removed the sputtered surface and restored the surface to a nearly perfect condition. The specimen was then warmed from 30 to 90K at a rate of ∿1.5K min^{-1} while being continuously photographed. No SIA contrast effects were observed during this experiment indicating that no SIAs crossed the surface. Previous work in our laboratory (14,15,16) indicates that if SIAs were present in the specimen, they would have appeared throughout the entire temperature range in this experiment; i.e. 30 to 95K. Thus we may conclude that no SIAs and hence no vacancies were produced by the irradiation. Unfortunately no contrast effects which could be associated with the arrival of helium interstitials at the surface were observed. This is not surprising in view of contrast mechanisms for SIAs (17).

In an effort to determine the temperature at which helium interstitials migrate, irradiations were performed at 48 and 92K. The composition profiles for these runs are shown in Fig. 17 and indicate that while helium is retained in the material at 48K in agreement with the results shown in Fig. 13, at 92K the level of detected helium is greatly reduced and is essentially at the level shown in the controls of Fig. 13. This result indicates that helium interstitials become mobile between 48 and 92K. These results are in rough agreement with the work of Wilson and Bisson (18) who calculate a migration energy of ∿0.25eV. A migration energy of ∿0.25eV would correspond to a migration temperature of ∿110K.*

* This is the temperature where the flux of SIAs to the surface would be a maximum.

Figure 17. Helium composition profiles for tungsten irradiated at 48K and 92K. The decreased concentration of He in the 92K irradiation versus the 48K irradiation indicates that helium interstitials become mobile between 48 and 92K.

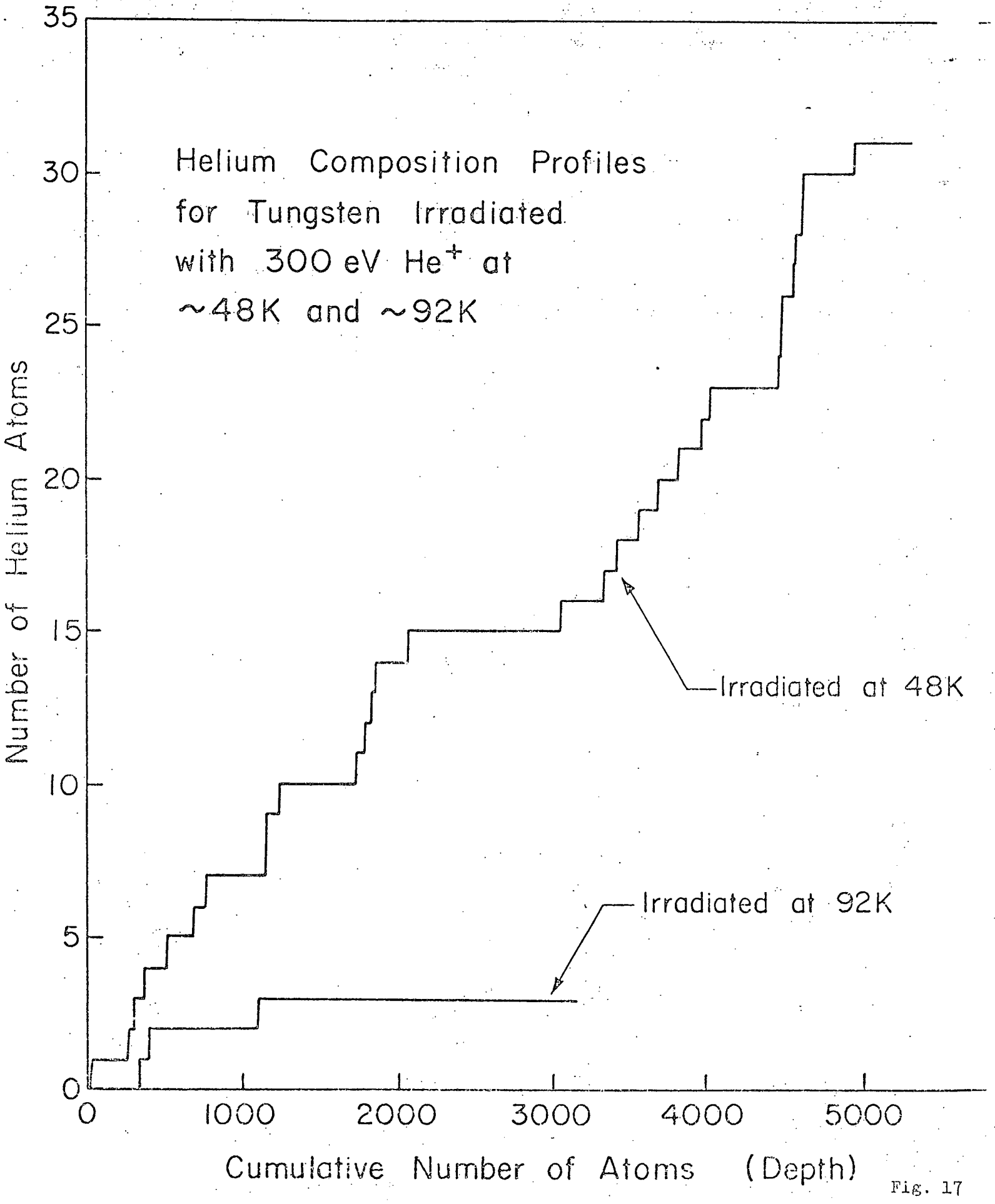
Helium Composition Profiles
for Tungsten Irradiated
with 300 eV He^+ at
~48K and ~92K
Irradiated at 48K
Irradiated at 92K
Number of Helium Atoms
Cumulative Number of Atoms (Depth)
0
5
10
15
20
25
30
35
0
1000
2000
3000
4000
5000

Fig. 17

Furthermore, the thermal desorption work of Kornelson* indicates that helium is not retained in tungsten irradiated with low energy helium at ~100K, thus placing the migration temperature below 100K.

4. Helium bubbles in molybdenum

The behavior of helium in metals has been a subject of increasing scientific interest because of its relevance to fusion reactor technology (19). The first wall of fusion reactors will be exposed to a high flux of relatively low-energy (<100keV) helium ions during their operation. The agglomeration of injected helium atoms, formation of helium bubbles and surface blisters will take place as a consequence of the injection of helium atoms. Surface blisters and helium re-emission phenomena have been investigated extensively by using electron microscopy and the thermal re-emission technique (20,21). However, formation of helium bubbles and growth mechanisms are not well understood (22).

Because of the unique capability of the atom-probe FIM with respect to both its atomic resolution for structural and compositional analysis, a more detailed study of the initial stage of helium bubble formation, including bubble density, size and internal gas pressure of bubbles, as well as the damage structure of the host lattice, is in progress.

Some initial investigation of helium bubbles in molybdenum has been carried out by the FIM in the following manner. Molybdenum FIM tips are first electropolished by a conventional method and then developed to a desired radius of curvature by the field-evaporation technique inside the FIM. The molybdenum tips are then removed from the FIM and placed inside a Faraday cage in a high-intensity irradiation port of the Hill-Nelson type ion-accelerator system. The irradiation is carried out with 20 to 40keV He^+ ions at room temperature. The total helium dose is varied from $5x10^{16}$ to $3x10^{17}$ ions cm^{-2} to obtain a high density of helium bubbles. The irradiation angles are varied to allow most of injected helium atoms to arrive within reasonably sharp tip. To date an initial investigation of the helium bubbles and damage structure has been conducted by using conventional FIM techniques. The chemical composition and spatial distribution of helium bubbles and the number of helium atoms inside the bubbles will be investigated in the near future by the atom-probe FIM.

---

* Private communication with E. V. Kornelson.

C. The Point-Defect Structure of Depleted Zones (Dr. M. Current and C-Y. Wei)

During the past year we have revived our earlier work (23,24,25,26) on the point-defect structure of depleted zones* (displacement spikes). The FIM is, at present, the only experimental technique capable of studying the point defect structure of depleted zones. The subject of the point-defect structure of a depleted zone (DZ) is basic to our knowledge of the damage produced by a single primary knock-on atom (PKA). The only other "technique" capable of giving detailed information about the detailed structure of a DZ is the computer simulation technique; this approach is a theoretical one and hence it is sensitive to the choice of the interatomic potential and the mathematical approximations employed.

In the present program of studies the emphasis is on determining: (1) the average number of vacancies produced by an ion incident with a given amount of energy; (2) the spatial distribution of vacancies within a depleted zone for an ion of a given mass; (3) the change in the spatial distribution of vacancies within a depleted zone as a function of the mass of the irradiating ion at constant bombardment energy; (4) the vacancy concentration within depleted zones; and (5) the effect of interstitial impurities on the average number and the spatial arrangement of vacancies within a depleted zone.

1. Technical improvements related to this subject

a. Faraday cage with channel electron multiplier array (CEMA)

A special Faraday cage, employing a channel electron multiplier array (CEMA) has been constructed to simultaneously measure the dose and observe visually the profile of the beam; Fig. 18 shows a cross-sectional view of the Faraday cage. The incident ion beam is first allowed to pass through an annular aperture (the secondary-electron retarder) which is biased at -300Vdc; this aperture defines the cross-section of the beam. The ion-beam then passes into the secondary-electron collection-cylinder and impinges on the top surface of the CEMA which is allowed to float; the CEMA serves to both collect the positive ion-beam and as an image intensifier. The ion current is converted to an electron current by the CEMA. The bottom surface of the CEMA is maintained at +900Vdc; this yields a gain of 10^4. The electron current is extracted from the CEMA by a +1500Vdc potential which is maintained on a phosphor screen that is deposited on a tin oxide coating that covers a glass plate. The extracted and accelerated electron beam is converted

* We use the term depleted zone in preference to displacement spike, although the two terms are often used interchangeably in the scientific literature.

Figure 18. A cross-sectional view of the Faraday cage used to both measure the positive ion current and observe the profile of the ion beam simultaneously. Note the CEMA and phosphor screen at the bottom of the figure.

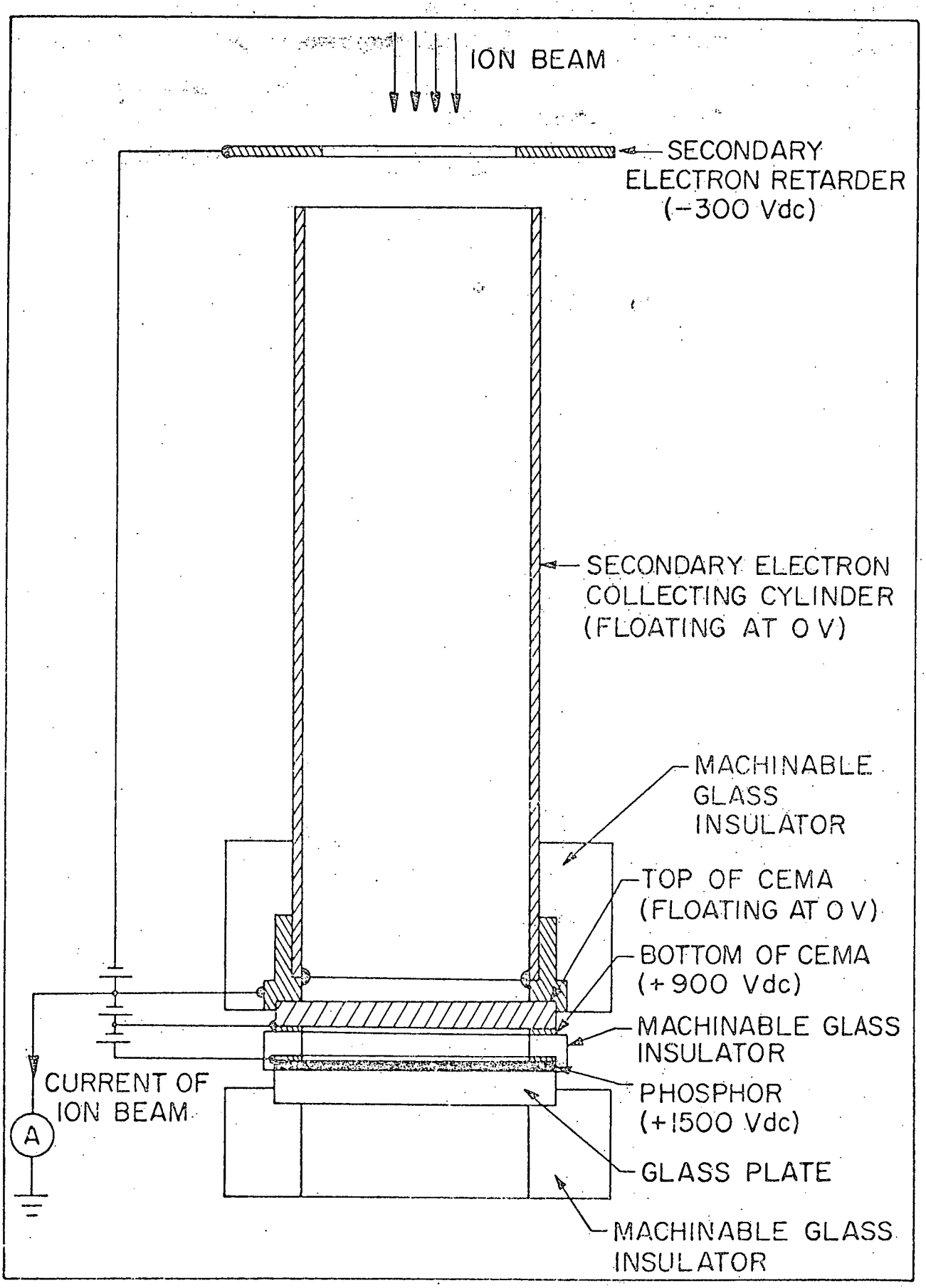
ION BEAM
SECONDARY ELECTRON RETARDER (-300 Vdc)
SECONDARY ELECTRON COLLECTING CYLINDER (FLOATING AT 0 V)
MACHINABLE GLASS INSULATOR
TOP OF CEMA (FLOATING AT 0 V)
BOTTOM OF CEMA (+900 Vdc)
MACHINABLE GLASS INSULATOR
PHOSPHOR (+1500 Vdc)
GLASS PLATE
MACHINABLE GLASS INSULATOR
CURRENT OF ION BEAM
A

Fig. 18

into visible light by means of the phosphor. In the above manner the positive ion beam is made visible for inspection.

The ion current is extracted from the top surface of the CEMA and is measured with an electrometer. The Faraday cage is insulated from the surrounding wall by two pieces of Corning machinable glass. Initial tests showed that the leakage current is less than 3×10^{-12} amp; this value is negligible in comparison to the minimum ion current of 1×10^{-10} amp used in a typical irradiation.

b. The use of a Houston omnigraphic 2000 x-y recorder with the Vanguard motion analyzer

To reconstruct a depleted zone in three-dimensions from the 35mm FIM micrographs it is necessary to determine the position of each vacant lattice site and its relationship to the surrounding perfect lattice site. The reconstruction process is accomplished with the aid of a Vanguard motion analyzer which has been interfaced to a Houston omnigraphic 2000 x-y recorder. The Vanguard motion analyzer has a pair of x-y crosshairs which are used to determine the position of a vacancy or an atom. The displacement of the crosshairs from a zero point (fixed by the investigator) is linearly proportional to a voltage which is used to initiate the pen of the x-y recorder. For a given depleted zone the positions of all the atoms surrounding the vacancies in a given plane are transferred to a sheet of graph paper mounted on the x-y recorder. This procedure is repeated for all the atomic planes passing through the region of the depleted zone. The information transferred to the graph paper is then used to reconstruct the depleted zone employing the Nova 1220 computer.

c. The application of the Oak Ridge Thermal-Ellipsoid Plot Program (OR TEP) to the visual display of depleted zones

The OR TEP program (27) was developed at Oak Ridge National Laboratory to provide three-dimensional and stereo-displays of large complex organic and biological molecules. We have applied this program to display the vacancy structure of depleted zones. The Prime computer in the Cornell Materials Science Center Computer Facility was used for the required calculations and plotting.

2. Results on a depleted zone in a Pt-4.0 at.% Au alloy

FIM specimens of a Pt-4.0 at.% Au alloy were irradiated at 40K with a 30keV W^+ ion beam to a dose of $\sim 1 \cdot 10^{13}$ ion cm^{-2}. After the 40K irradiation each specimen was annealed isochronally to 100K, then cooled back to 70K where it was pulsed field evaporated atom-by-atom to detect the presence of vacancies and interstitials. In only one out of three specimens did we find a mapable and isolated

depleted zone in the bulk of a specimen; it had an average radius of curvature of ∿190A. We refer to this depleted zone as DZA; its position in the FIM tip, relative to the two other depleted zones detected in the tip is shown in Fig. 19. It is noted that DZA is located ∿30A down from the initial surface and ∿90A from the irradiated surface of the specimen. Depleted zone B is located near the $(93\bar{1})$ plane and depleted zone C is located near the $(2\bar{2}0)$ plane. Depleted zones B and C were found only one or two interplanar spacings from the irradiated surface of the specimen.

Depleted zone A detected in the $(75\bar{1})$ plane was found to consist of 31 vacant lattice sites clustered in a disc-shaped region, ∿20A in diameter lying near a $(\bar{2}\bar{2}0)$ plane. Fig. 20 shows a series of ten FIM micrographs of ten successive $(75\bar{1})$ planes; they were chosen from a total of $1.2\text{x}10^3$ frames of 35 mm ciné film which were recorded and analyzed in the reconstruction of DZA. The $(75\bar{1})$ plane and the surrounding planes are indexed in frame 1; the frame number of the ciné film is located in the lower right-hand corner below each micrograph and the layer number is preceded by the letter n in the upper left-hand corner above each micrograph. The position of every atom in the $(75\bar{1})$ plane is indicated schematically below each micrograph by a solid black circle and a vacant lattice site is indicated by an open circle. Frames 112, 348, 392, 519, 640 and 711 exhibit vacant lattice sites in layers 2, 5, 6, 7, 8 and 9 respectively. Figs. 21(a), 21(b) and 21(c) show the projection of the vacant lattice sites contained in DZA onto the $(0\bar{1}0)$, (100) and (001) planes respectively. The projection onto the (001) planes, in Fig. 21(c) shows very clearly that the habit plane is a $(\bar{2}\bar{2}0)$ plane. Fig. 21 is a photograph of a ball-model of DZA; each ball represents a vacant lattice site and the surrounding lattice atoms have been omitted for clarity. The photograph in Fig. 21 was taken along approximately a $[\bar{1}00]$ direction.

A three-dimensional plot of DZA is shown in Fig. 22; this plot was made via the OR TEP program. The circles represent the vacant lattice aites and the length of the connecting bonds between vacant lattice sites is equal to the first nearest-neighbor distance in the face-centered cubic lattice. The viewing direction in Fig. 22 is approximately along an $[01\bar{1}]$ direction. It is clear from this figure that the morphology of DZA is very close to that of a cylindrical vacancy cavity.

The calculation of the vacancy concentration in a depleted zone involves a degree of unertainty as one must always estimate, in some manner, the number of atoms associated with the depleted zone. Two procedures were adopted for estimating the vacancy concentration (c_v). In the first procedure we define, in a

Figure 19. (a) A 200 stereographic projection showing the positions of depleted zones A, B and C; (b) A side view of the FIM tip showing the geometric relationship of depleted zones A, B and C.

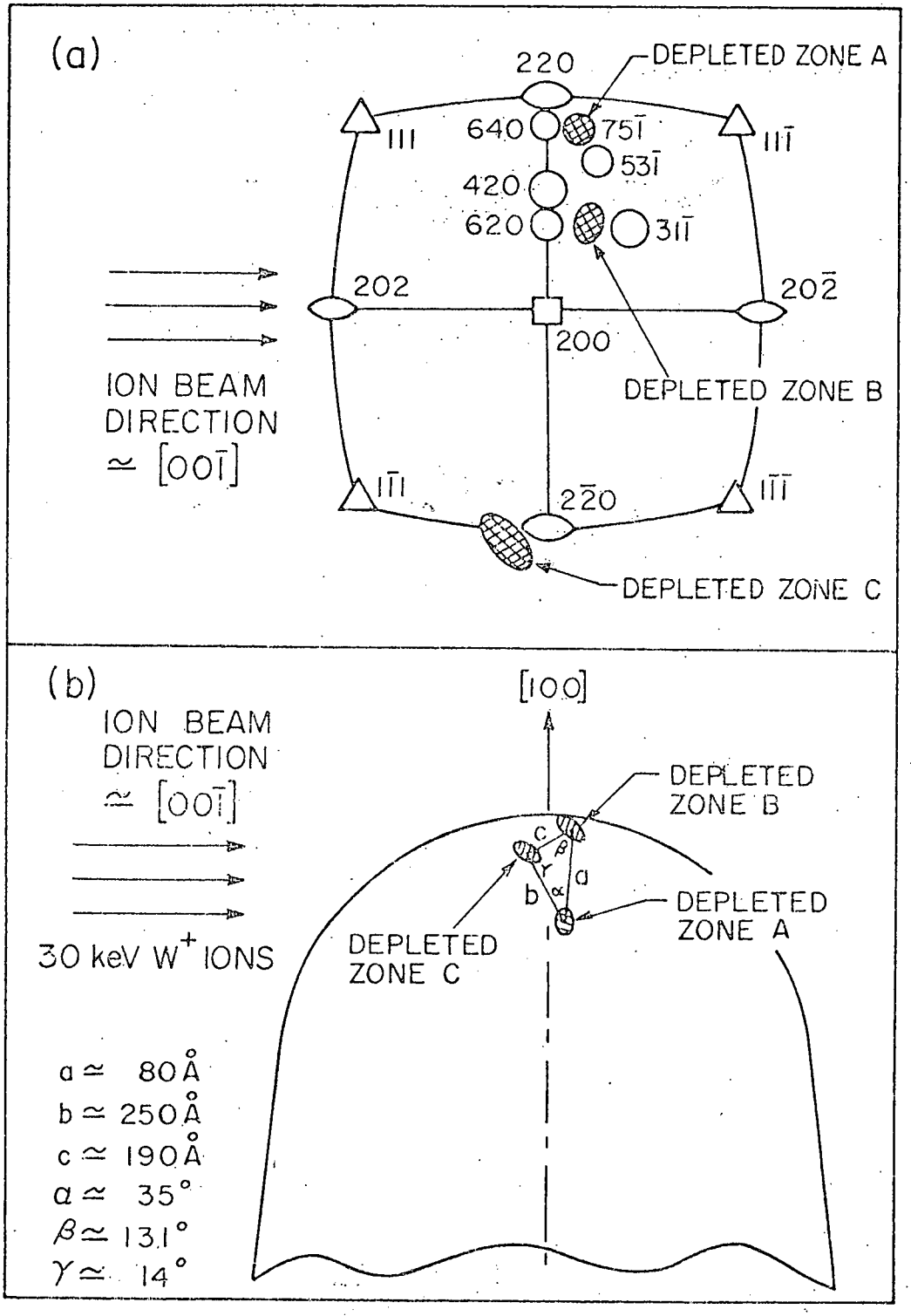
(a)
220
DEPLETED ZONE A
111
640
75$\bar{1}$
11$\bar{1}$
53$\bar{1}$
420
620
31$\bar{1}$
202
20$\bar{2}$
200
ION BEAM
DIRECTION
≃ [00$\bar{1}$]
DEPLETED ZONE B
1$\bar{1}$1
2$\bar{2}$0
1$\bar{1}$$\bar{1}$
DEPLETED ZONE C
(b)
[100]
ION BEAM
DIRECTION
≃ [00$\bar{1}$]
DEPLETED
ZONE B
c
β
γ
a
b
α
DEPLETED
ZONE A
DEPLETED
ZONE C
30 keV W+ IONS
a ≃ 80 Å
b ≃ 250 Å
c ≃ 190 Å
α ≃ 35°
β ≃ 13.1°
γ ≃ 14°

Fig. 19

Figure 20. A series of 10 FIM micrographs out of 898 showing the vacant lattice sites (open circles) contained within depleted zone A detected in the $(75\bar{1})$ plane; the solid circles indicate lattice atoms.

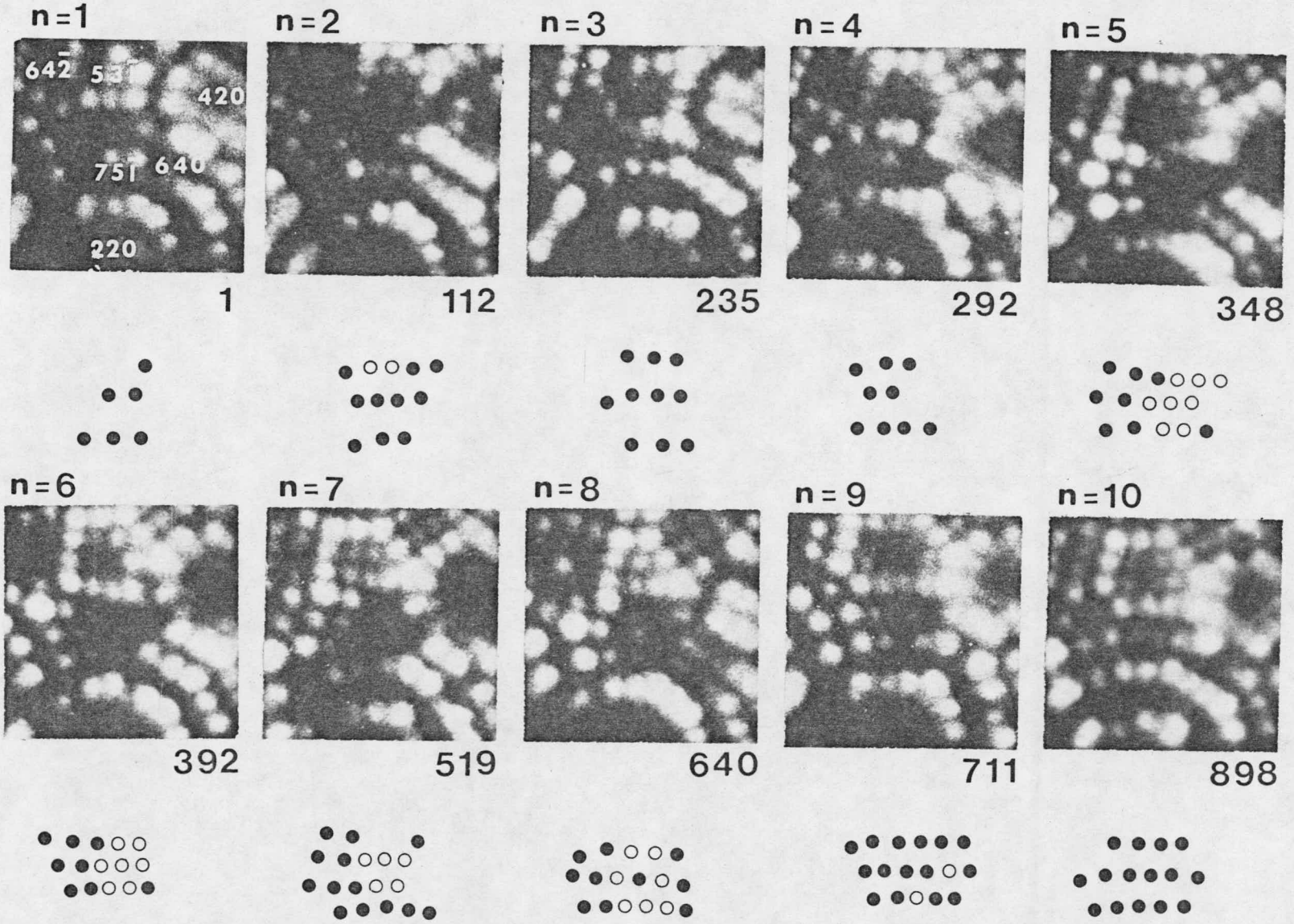
n=1
642
420
751
640
220
1
n=2
112
n=3
235
n=4
292
n=5
348
n=6
392
n=7
519
n=8
640
n=9
711
n=10
898

Fig. 20

Figure 21. (a), (b) and (c) represent the projection of the vacant lattice sites in depleted zone A onto the $(0\bar{1}0)$, (100) and (001) planes respectively; (d) shows a photograph of a ball model of the depleted zone taken along the $[\bar{1}00]$ direction.

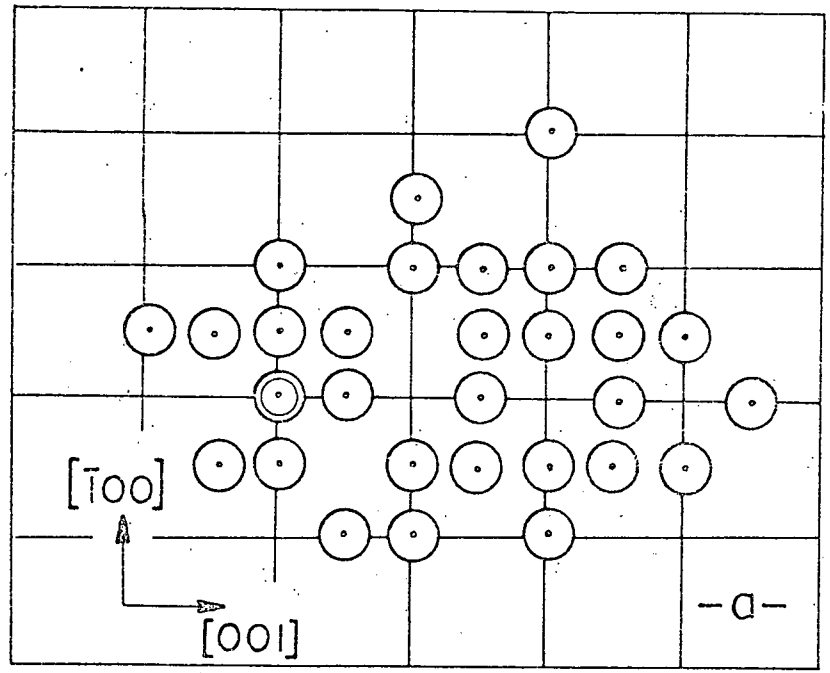

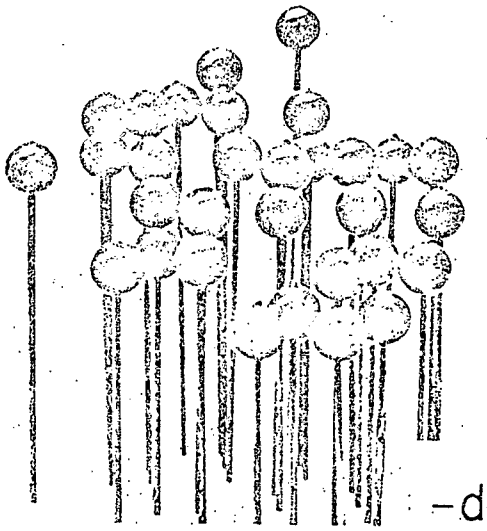

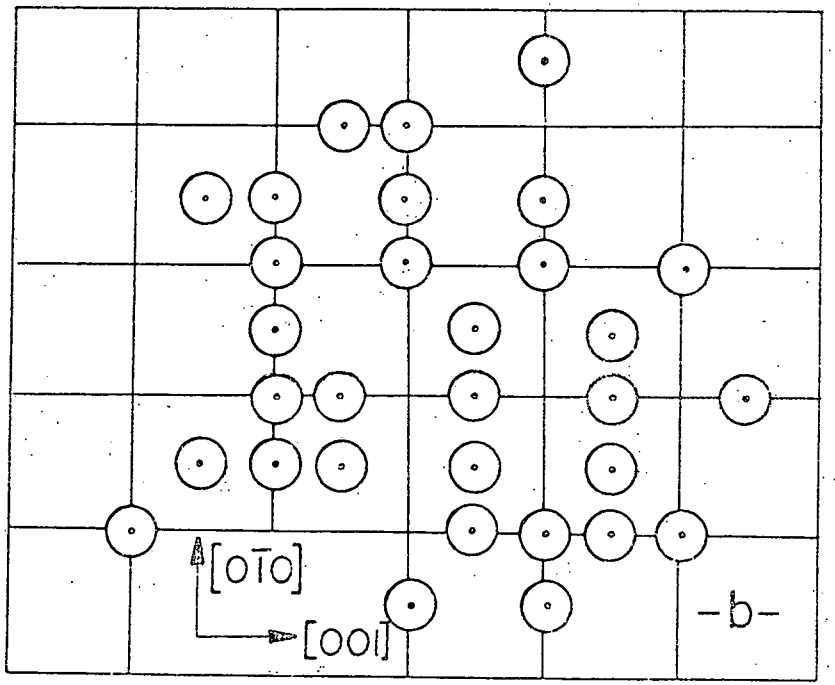

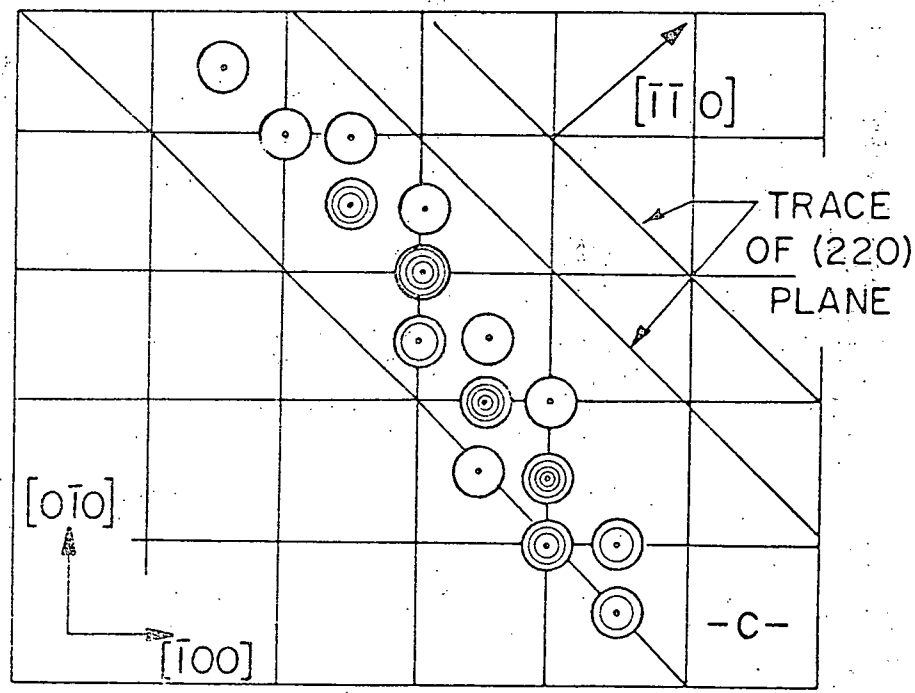

Fig. 21

Figure 22. An isometric drawing of depleted zone A made with the aid of the OR TEP program. The viewing direction is approximately along the [0$1\bar{1}$] direction.

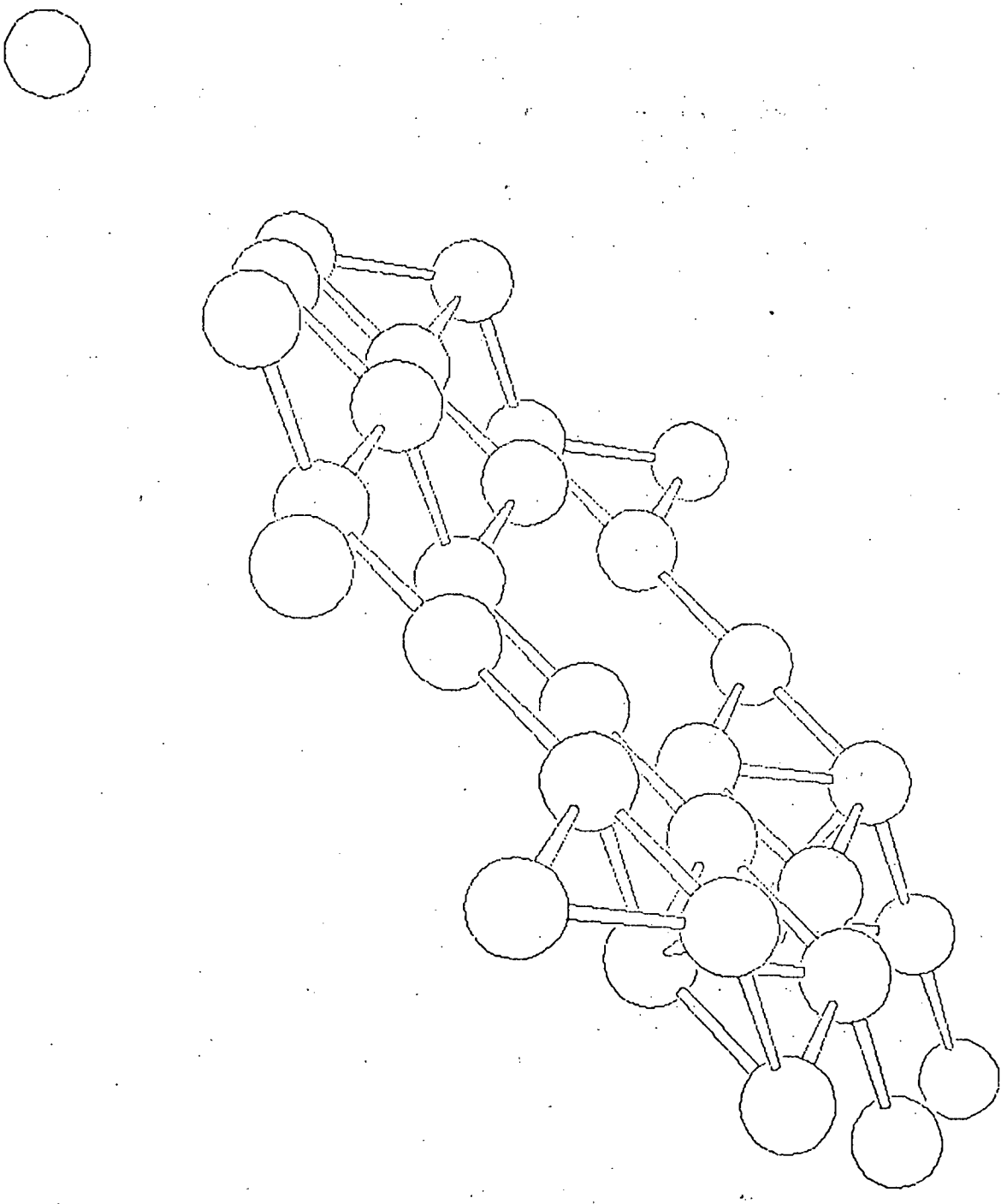

Fig. 22

reasonable manner, a volume containing the depleted zone and then calculated c_v. the second procedure involved calculating c_v in each x-y plane and then averaging over all x-y planes contained within the depleted zone. This procedure was repeated for the y-z and z-y planes. The three values of c_v were then averaged. The possible range of c_v employing the above two counting procedures for the DZA is ∿35 to 44 at.%.

If only first nearest-neighbors vacant lattice sites are considered, then the size distribution of clusters is as follows: (1) two monovacancies, and (2) one jumbo vacancy cluster containing 29 vacancies. This cluster size distribution shows that DZA is, indeed, very compact. It is our opinion that DZA corresponds to a cylindrical vacancy cavity and that this is the precursor state before collapse into a lower energy prismatic dislocation loop. Transmission electron microscope studies (28) on neutron irradiated platinum have shown that such loops do exist.

3. Results on tungsten irradiated with 30keV Cr^+, Mo^+ or W^+ ions

Specimens of four-pass zone-refined tungsten wires [resistivity ratio between room temperature and 4.2K of ≃ $(1.5\text{-}3)\cdot 10^4$] were irradiated <u>in-situ</u> at 14 to 18K at a pressure of less than $1\cdot 10^{-8}$ torr to a total dose of ∿$1\text{x}10^{13}$ ion cm^{-2} with 30keV Cr^+, Mo^+ or W^+ ions. Each irradiated specimen was pulsed field-evaporated atom-by-atom at 14 to 18K to search for both vacancies and self-interstitial atoms (SIAs).

To date we have only analyzed in detail the results from the specimens irradiated with 30keV Cr^+ ions; these results are reported here. In two of the four irradiated specimens we found three mapable depleted zones; they are denoted DZ-D, DZ-E and DZ-F. The depleted zones D and E were detected in the regions of the (222) and (411) poles respectively of one specimen. Depleted zone F was found in the region of the (222) pole of a second specimen. The DZ-D contains 513 vacant lattice sites and 6 SIAs contained within a volume ∿100A in diameter and ∿250A in length, DZ-E contains 258 vacant lattive sites located within a volume ∿120A in diameter and ∿200A in length and DZ-F consisted of 291 vacant lattice sites arrayed within a volume ∿70A in diameter and ∿200A in length. Each of these three depleted zones was most likely <u>not</u> created by a single incident ion; in particular note that depleted zone D exceeds the maximum possible Kinchin-Pease value of 300 by 213 vacant lattice sites.

The vacancy concentration (c_v) for each depleted zone was calculated in a manner similar to the one described in the previous section. In addition, c_v was also calculated by determining the average vacancy concentration in a slab five layers thick for the x-y, y-z and z-x planes; the average vacancy concentration

for the depleted zone was then determined by averaging the concentration in all the five-layer thick-slabs. The value of c_v calculated in this manner is, typically, less than the value of c_v determined by the method of the previous section by a factor of two to four. This result is, simply, due to the larger number of lattice sites included in the second method of calculating c_v. The two different values of c_v calculated by the different definitions shows the possible range of c_v in depleted zones.

In Fig. 23 we compare the average vacancy concentration in DZ-D, DZ-E and DZ-F with the c_v calculated for the depleted zone produced by a 20keV W^+ ion in W and reported earlier by Beavan et al. (29); the Beavan et al. data was re-analyzed by the methods discussed in this report. It is clear from the data exhibited in Fig. 23 that the value of c_v produced by a 30keV Cr^+ in W is significantly lower than the value of c_v produced by a 20keV W^+ ion in W. Additional experiments are in progress to obtain the values of c_v for depleted zones produced by 30keV Al^+ and Mo^+ ions.

We have also determined a radial distribution function R(i) and a normalized radial distribution function P(i) for each depleted zone. The quantity R(i) is defined as the average number of vacant lattice sites in the i^{th} spherical shell around a vacancy; the i^{th} shell is located between the sphere with radii r_{i-1} and r_i. The quantity R(i) is given by

$$R(i) = \sum_{j=1}^{N_t} N_v(i,j)/N_t \qquad (1)$$

where $N_v(i,j)$ is the number of vacant lattice sites in the i^{th} shell measured from the j^{th} vacant lattice site and N_t is the total number of vacant lattice sites in the depleted zone. The normalized radial distribution function P(i) is then given by

$$P(i) = \sum_{j=1}^{N_t} N_v(i,j)/N_t(N_t-1). \qquad (2)$$

Figs. 24 and 25 show P(i) calculated for DZ-F and the 20keV depleted zone detected by Beavan et al. (29) respectively. In the calculations for Figs. 24 and 25 the thickness of each shell was taken to be equal to $2.5a_o$, where a_o is the lattice parameter of tungsten. It is clear from these two figures that the depleted zone produced in W by a 20keV W^+ ion is considerably more compact than the one produced by a 30keV Cr^+ in W.

Figure 23. The average vacancy concentration in different depleted zones in tungsten produced by 30keV Cr^+ ions or 20keV W^+ ions.

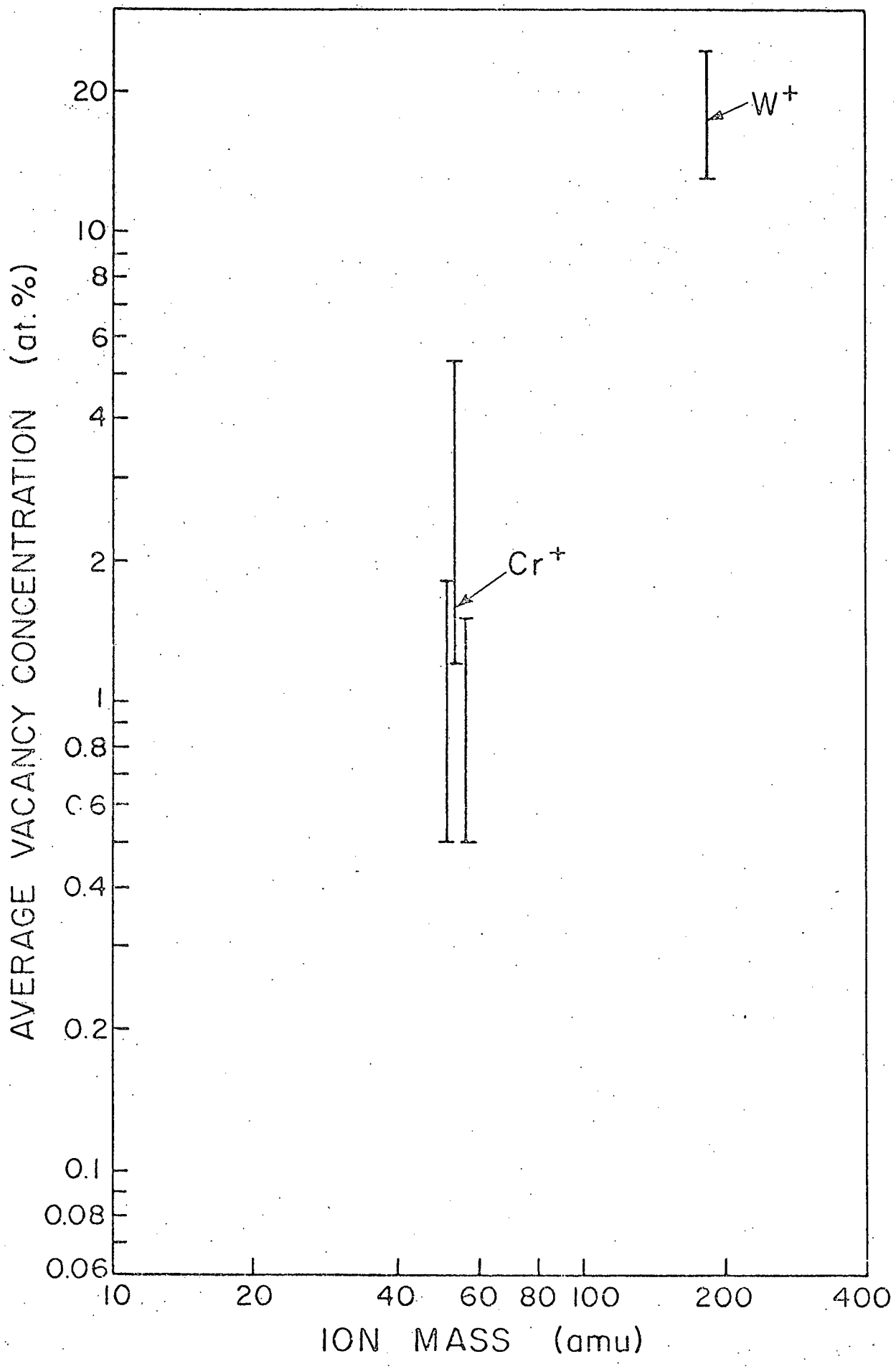
AVERAGE VACANCY CONCENTRATION (at.%)
20
10
8
6
4
2
1
0.8
0.6
0.4
0.2
0.1
0.08
0.06
W+
Cr+
10
20
40
60
80
100
200
400
ION MASS (amu)

Fig. 23

Figure 24. The normalized radial distribution function (Eq. 2) as a function of distance for DZ-F. The thickness of each shell is taken as $2.5a_o$, where a_o is the lattice parameter of tungsten.

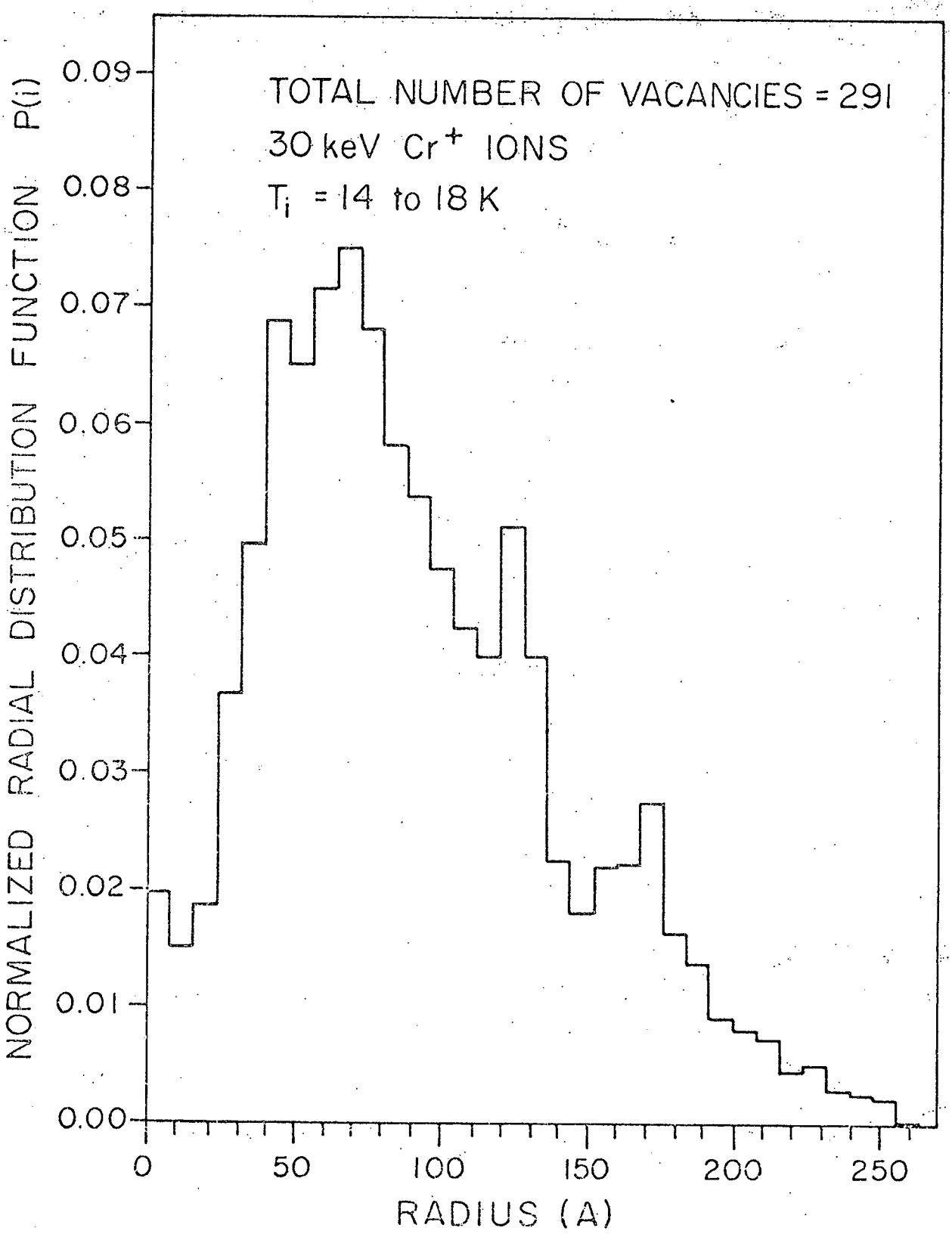
TOTAL NUMBER OF VACANCIES = 291
30 keV Cr+ IONS
Ti = 14 to 18 K
NORMALIZED RADIAL DISTRIBUTION FUNCTION P(i)
0.09
0.08
0.07
0.06
0.05
0.04
0.03
0.02
0.01
0.00
0
50
100
150
200
250
RADIUS (A)

Fig. 24

Figure 25. The normalized radial distribution function P(i) calculated for the depleted zone detected by Beavan et al.

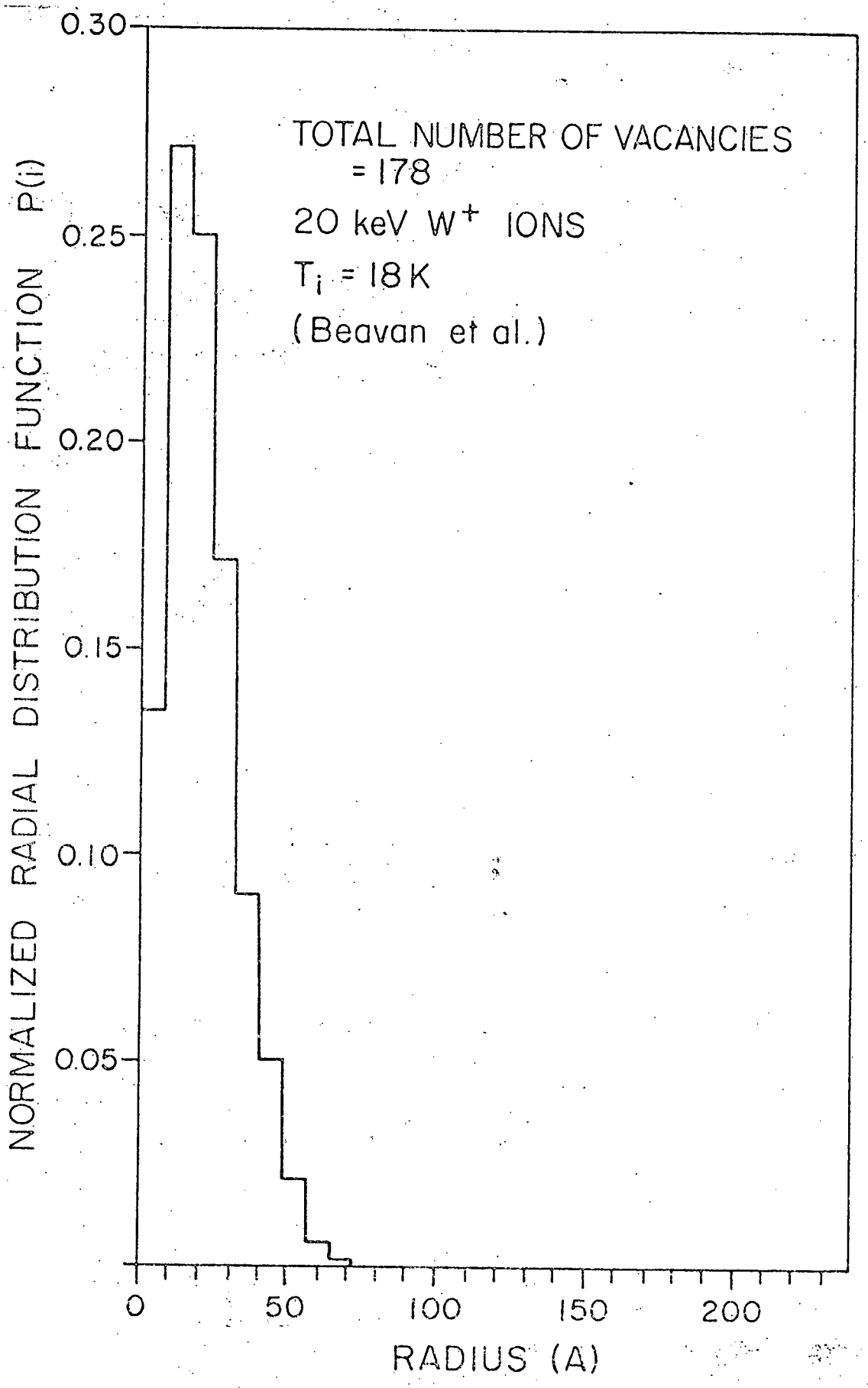
TOTAL NUMBER OF VACANCIES
= 178
20 keV W+ IONS
Ti = 18 K
(Beavan et al.)
NORMALIZED RADIAL DISTRIBUTION FUNCTION P(i)
0.30
0.25
0.20
0.15
0.10
0.05
0
50
100
150
200
RADIUS (A)

Fig. 25

4. Influence of interstitial nitrogen on self-ion damage in tantalum

Recent transmission electron microscope (TEM) studies of the self-ion damage in bcc molybdenum (30) show a dramatic decrease in the defect yield (number of damage regions visible within the TEM image for a given dose) and damage efficiency (fraction of vacancy self-interstitial atom pairs which survive recombination) with the addition of ∿17appm interstitial nitrogen to zone-refined molybdenum. A lattice dynamics calculation for the case of interstitial carbon in α-iron (31) lends detailed support to the suggestion that the presence of carbon interstitial-metal complexes in the lattice can supress the initial separation of vacancy-self-interstitial atom pairs. A decrease in the average range of replacement collision sequences then encourages a higher recombination rate and reduces the amount of surviving damage. Preparations are being completed for a study of the initial state of damage in tantalum (as a complement to the more thoroughly investigated case of tungsten) and a systematic survey of the effect of interstitial gas solutes in the range of a few appm to ∿5 at.% on the nature of the initial and annealed self-ion damage.

a. Experimental preparation

1) The vacuum outgassing and quenching system has been upgraded and expanded to the point where 15 cm segments of high purity wire can be outgassed in vacuum and then doped by rapid radiation quenching to obtain a known fraction of interstitial gases. The system can now be used to prepare Ta(O) and Ta(N) solutions up to the range of ∿5 at.%.

2) In order to establish the careful calibration of the irradiation beam dose needed for useful comparisons between the damage produced in various metal-gas solutions, a combined Faraday cage-channel plate assembly has been fabricated at the Clark Hall machine shop. This design, which is similar to the one described earlier in this section, allows for a continuous and simultaneous monitoring of the ion beam profile as well as the beam intensity and total irradiation dose.

3) The development of an effective and reliable electropolishing procedure for producing FIM tips of tantalum is a more problematical task than for the case of tungsten or molybdenum. Most published solutions for tantalum (see Table 1) have a tendency to produce strongly deformed-end regions and depend sensitively on solution histroy and the polishing potential. The polishing properties of a given solution and polishing routine also depend on the form of tantalum

Table 2. Solutions for electropolishing tantalum and tantalum (nitrogen) alloys.

Solution	Potential (Vdc)	Tip Quality	Notes
13 ml HF 7 ml H_2SO_4 7 ml H_3PO_4 3 ml CH_3COOH	10-15	rough edges diameter ∿2000A	a
10 ml HF 10 ml H_2SO_4 5 ml H_3PO_4 5 ml CH_3COOH	10-15	uneven profile diameter ∿500-1000A	b
15 ml H_2SO_4 10 ml HF 5 ml H_3PO_4	12-15	smooth taper, nippled tip profile diameter ∿800-1600A	
15 ml HF 15 ml H_2SO_4 2 ml HCl	2-7	long narrow taper, some jagged edges at tip diameter ∿500-1000A	c
15 ml HF 10 ml H_2SO_4 5 ml H_3PO_4	6-10	jagged edges at tip diameter ∿1200A	
13 ml HF 10 ml H_2SO_4 5 ml H_3PO_4 2 ml CH_3COOH	3-7	severe "saw-tooth" edges, narrow tip diameter ∿400A	d

a) This is Müller's solution. Very active etching reaction.

b) The middle of the road solution from Ishimura's survey of acid combinations using only optical microscope examination of tip profile. This gives a generally more even etch than Müller's.

c) Froths up vigorously when the HCl is added to the other two. Solution "ages" rapidly - with the later etch tips getting a more even removal of material for a given etch potential.

d) This variation on Müller's solution is even more unstable than the original and gives a very uneven attack along the thinnest section of the tip.

wire used: (1) "off-the-roll" MRC Marz-grade tantalum; (2) outgassed wire (characterized by a grain length which is from 1 to 10 times the wire diameter; and (3) outgassed and quench-doped tantalum-interstitial solutions. The polishing rates at the grain boundary, for example, are considerably less than the rates along the sides of the segments themselves. This produces a sequence of knobs and facets as the wire end is thinned rather than the smooth taper to a point which is characteristic of tungsten. An additional complication is the tendency for tantalum to form an oxide layer over the tip and the case at which the tip can be charged with interstitial hydrogen from acidic solutions (this fact precludes the use of any etching routines).

A systematic survey of the etch solutions listed in Table 2 and their modifications is continuing. Tip profiles of the three types of tantalum specimens are first checked with a 400X optical microscope and then in a 100keV (120,000X) scanning electron microscope. The SEM is particularly useful for following the effects of polishing voltage and routines on the end forms of the wire tip. Several etched wires have been imaged in the ion-accelerator FIM system. A smaller FIM assembly is presently being rehabilitated as a tip test stand for this project.

D. Recovery in Stage II of Ion-Irradiated Pt(Au) Alloys: An Up-Date

Direct and visible evidence has been obtained for long-range migration of self-interstitial atoms (SIAs) in Stage II of three different ion-irradiated platinum (gold) alloys. Field-ion microscope (FIM) specimens of Pt-0.10, 0.62 and 4.0 at.% Au alloys were irradiated <u>in-situ</u> with 30keV W^+ or Pt^+ ions at a tip temperature of 35 to 41K at $2 \cdot 10^{-9}$ torr. Direct observation of the surfaces of the FIM specimens during isochronal warming experiments to 100K showed that a flux of SIAs crossed the specimens' surfaces between 40 to 100K. The spectrum for each alloy consisted of two recovery peaks centered at ~60 and 88K (substages II_B and II_C). The position of substage II_B exhibits a systematic dependence on the gold concentration (c_{Au}) (see Fig. 25).

The recovery between 40 and 100K can be explained on the basis of an impurity delayed diffusion model. When kT becomes sufficiently large the SIAs are able to detrap from the Au atoms and to migrate through the lattice. During their course of migration through the lattice the SIAs retrap and detrap at Au atoms until they finally reach the surface of the FIM specimen where they are observed as an extra

Figure 26. The composite isochronal recovery spectra of the Pt/0.10 at.% Au, Pt/0.62 at.% Au and the Pt/4.0 at.% Au alloys which were irradiated between 35 and 40K with 30keV W^+ or Pt^+ ions and then warmed to 100K at a linear rate of ~1.5K/min.

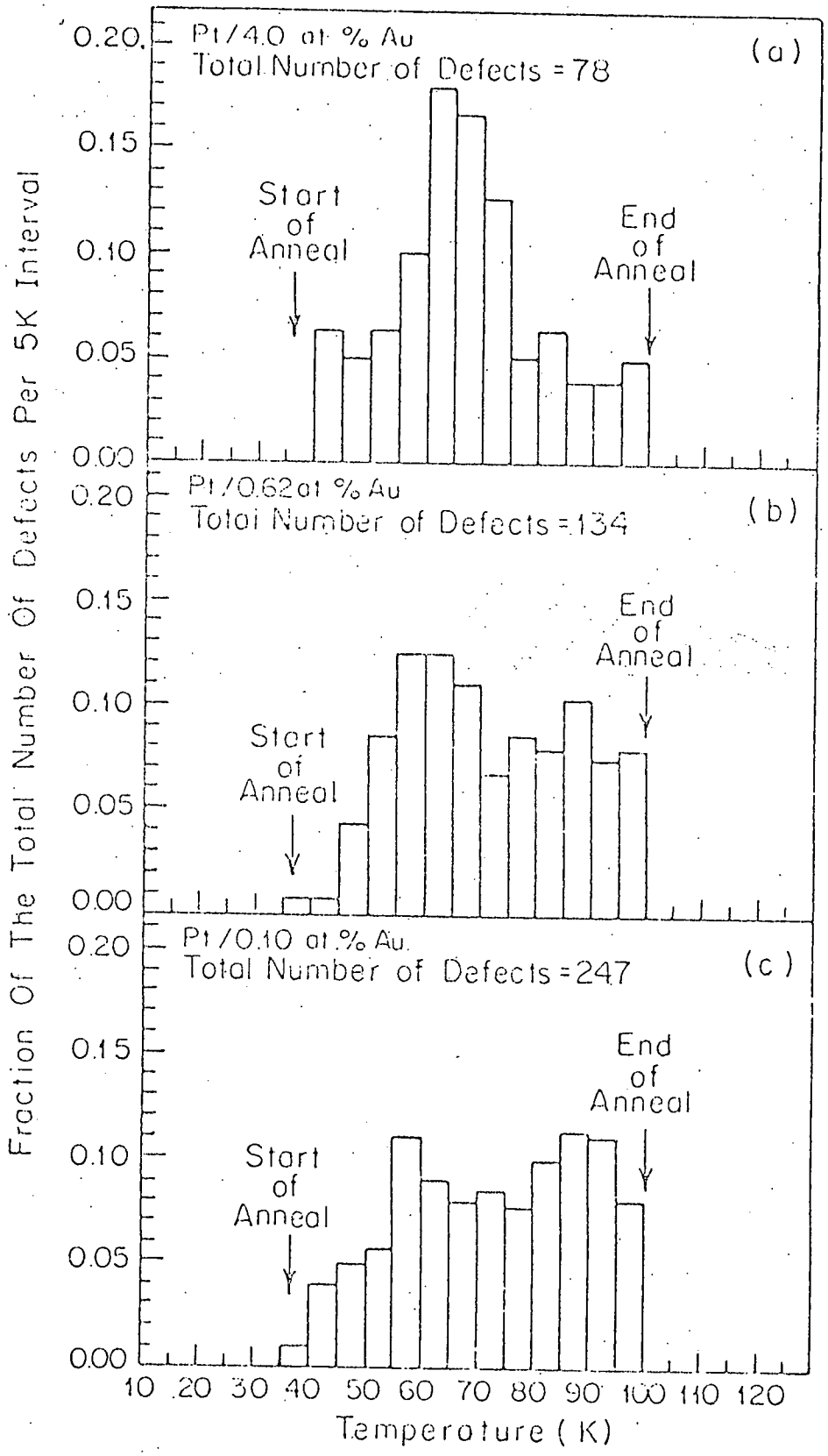
Pt/4.0 at % Au
Total Number of Defects = 78
(a)
Start of Anneal
End of Anneal
Pt/0.62 at % Au
Total Number of Defects = 134
(b)
Start of Anneal
End of Anneal
Pt/0.10 at % Au
Total Number of Defects = 247
(c)
Start of Anneal
End of Anneal
Fraction Of The Total Number Of Defects Per 5K Interval
0.00
0.05
0.10
0.15
0.20
10 20 30 40 50 60 70 80 90 100 110 120
Temperature (K)

Fig. 26

bright-spot in the FIM image. The number of retrapping and detrapping events increases as c_{Au} increases and concomitantly the effective diffusion coefficient of the SIA decreases as $1/c_{Au}$ (32). Thus, the temperature at which the maximum in substage II_B occurs increases with increasing c_{Au}. The observation of two long-range migration recovery peaks in all three Pt(Au) alloys is incorporated into the inpurity-delayed diffusion description employing a two-level trapping model (32). Thus, it is assumed that at T_i the two trapping levels corresponding to substage II_B and II_C become occupied by the initially mobile SIAs to form two distinct configurations of immobile gold atom-SIA complexes. As kT is increased, from T_i, during the isochronal annealing experiment the SIAs trapped in the less-tightly bound state (II_B) are able to detrap and retrap from this state until they reach the surface of the FIM specimen. In addition, the SIAs in the less-tightly bound state are also capable of jumping into a more-tightly bound state (II_C). Finally, with a further increase in kT the SIAs in this more-tightly bound state are able to detrap and to give rise to substage II_C.

In Fig. 26 we compare the present work on the Pt/0.10 at.% Au with two isochronal recovery experiments on Pt(Au) alloys that employed electrical resistivity measurements. Fig. 26(b) exhibits the work of Shambra and Jackson (33) on both an annealed specimen and an annealed and pre-quenched specimen; the pre-quenching treatment seeds the specimen with vacancies prior to the low temperature irradiation. The enhanced recovery observed by Shambra and Jackson is indicative of long-range migration. Finally, Fig. 26(c) shows the results of Schilling et al. (34); we have omitted the substage II_A they detected since this occurred below the value of T_i we employed. The position of substage II_B in the Schilling et al. work (40K) is below our substage II_B, but this can be explained on the basis of the different damage pattern produced by electron irradiation.

E. The Range of a Focused Collision Replacement Sequence in Ordered Alloys (J. Aidelberg)

In a recent study of partially ordered Ni_3Mn irradiated with thermal neutrons Kirk et al. (35) claim to have developed a technique to measure the average length of a focused collision replacement sequence. These workers have measured the change in magnetic saturation with dose for different values of the long-range order-parameters(S). The change in magnetic saturation with dose was measured for S equal to approximately 0.79, 0.90 and 0.95. A quantitative computer analysis of

Figure 27. A comparison of our results [26(a)] on the Pt/0.10 at.% Au alloy with the isochronal recovery experiment of Shambra and Jackson [26(b)] and Schilling et al. [26(c)].

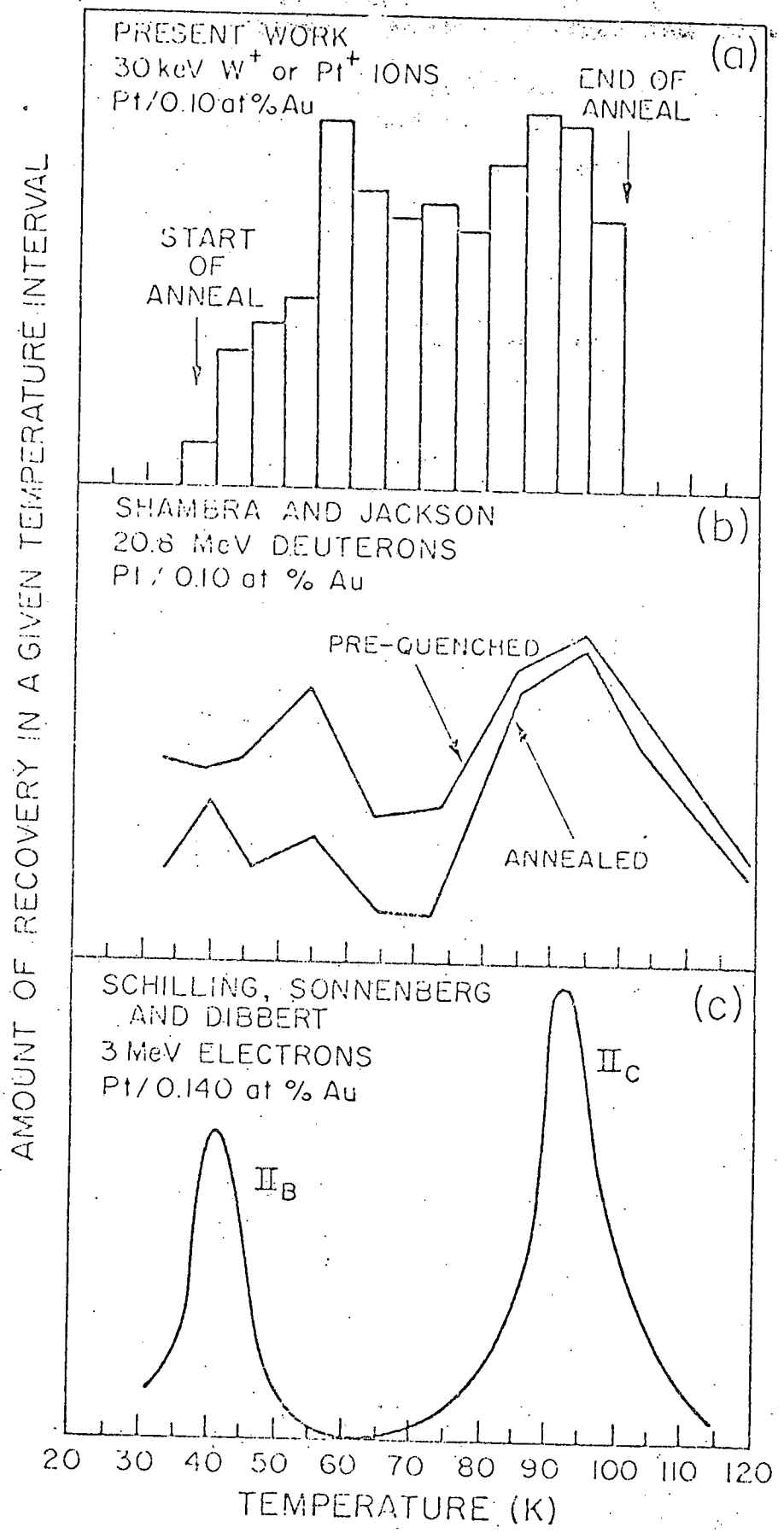
PRESENT WORK
30 keV W+ or Pt+ IONS
Pt/0.10 at % Au
(a)
END OF ANNEAL
START OF ANNEAL
SHAMBRA AND JACKSON
20.8 MeV DEUTERONS
Pt / 0.10 at % Au
(b)
PRE-QUENCHED
ANNEALED
SCHILLING, SONNENBERG AND DIBBERT
3 MeV ELECTRONS
Pt/0.140 at % Au
(c)
$I\!I_C$
$I\!I_B$
AMOUNT OF RECOVERY IN A GIVEN TEMPERATURE INTERVAL
20 30 40 50 60 70 80 90 100 110 120
TEMPERATURE (K)

Fig. 27

the magnetic disorder produced by <111> focused collision replacement sequences showed that the magnetic disorder caused by a focused collision replacement sequence is a maximum at S=0.7 and decreases to zero at S=1. Kirk et al. calculated from their data an average sequence length of about 50 atoms along the <110> direction.

We are presently studying the random disordering produced by focused collision replacement sequences in Ni_4Mo by direct observation in the FIM. The ideas pertinent to the experiment are as follows. If one starts with a fully ordered alloy (S=1) then the FIM image of this alloy resembles that of a pure metal (36,37). The result of the lattice disorder produced by the focused replacement sequences is to change the image contrast to that which is characteristic of a random alloy (37). A specimen of the fully ordered alloys is irradiated in-situ with low energy neon ions (<1000eV) so that all the vacancies are left at the irradiated surface and the interstitials are driven into the bulk of the FIM specimen by the focused collision replacement sequence mechanism. After the irradiation the specimen is pulsed field-evaporated and the measured width of the disordered region (as detected by its random appearance) is used as a measure of the range of the focused collision replacement sequence.

During the past year we expended a good deal of effort to obtain ordered specimens of Ni_3Mn and Ni_3Fe without too much success. The main problem appeared to be connected with specimen homogeneity. Hence, an extensive effort was made to control the stoichiometry and the uniformity of the composition of these two alloys. To this end we extensively employed wet chemistry and the atomic absorption techniques to determine the chemistry and x-ray fluoresence to insure homogeneity of the composition throughout the alloys. Wire specimens of these alloys are presently being heat-treated to produce the ordered alloys.

Considerable time was also spent in developing a reliable electropolishing technique for producing sharply pointed FIM specimens. The procedure developed is as follows: (1) a wire with a diameter of 0.02cm and 1 cm in length is dipped to a depth of 4mm into the electropolishing bath; (2) the electrolyte consists of a freshly made solution of 1 part H_2SO_4 to 20 parts Methanol (by volume) used at room temperature; and (3) five Vac is applied across the electrolytic cell and ∿2mm of metal is removed from the end of the specimen. At the end of the polishing treatment we obtain an FIM tip with a diameter of ∿50 to 100A.

A series of preliminary irradiation experiments on Ni_4Mo indicated that we needed: (1) a lower ultimate background pressure in the FIM; and (2) an ion-gun with a more intense ion beam. Thus, during the past year we improved the FIM to

obtain a background pressure of (4 to 5)x10^{-10} torr routinely. A low background pressure is necessary since we must irradiate the specimens in the absence of an electric field and at a pressure of $5 \cdot 10^{-10}$ torr very little impurity adsorption will occur during the relatively short irradiation periods (10 minutes). In addition we modified the ion-gun so that it is now similar to the one described in the section on the atom-probe FIM.

F. Invited Seminars and Papers

A number of invited seminars and papers were presented during the present contract year. They are as follows:

1. "The Study of Defects in Metals by Field-Ion Microscopy and Atom-Probe Microscopy", International Symposium on Application of Field-Ion Microscopy to Metallurgy, Lake Yamanaka, Japan, May 6-8, 1976.

2. "Application of the Field-Ion and Atom-Probe Microscopes to the Study of Defects", Third Annual Meeting of the Microscopical Society of Canada, Ottawa, Canada, June 1976.

3. "An Atom Probe Field-Ion Microscope for the Study of the Interaction of Impurity Atoms or Alloying Elements with Defects", Argonne National Laboratory Conference on "Properties of Defects in Metals", Argonne, Illinois, October 18-22, 1976.

4. A review paper for a Festschrift-type issue of Surface Science to honor the retirement of Professor Erwin W. Müller.

G. The Fast-Neutron Irradiation of Wire Specimens in EBR-II

A large number of wire specimens of tungsten, tungsten (rhenium), molybdenum, molybdenum (titanium), TZM, iron and iron (silicon) are presently being irradiated in EBR-II. The specimens are being irradiated with the help of Dr. M. Grossbeck of Oak Ridge National Laboratory (ORNL) (see pages 84-85 of the 1976 annual progress report of the Metals and Ceramics Division of the Oak Ridge National Laboratory) and Dr. J. J. Laidler of the Hanford Engineering and Development Laboratory (HEDL). The specimens in the ORNL capsules will not be ready until 1979, whereas we are hopeful to have the specimens from the HEDL capsules somewhere between January and July 1978.

III. OTHER FINANCIAL ASSISTANCE

A total of $9,749 will have been received from the National Science Foundation, through the Cornell University Materials Science Center, during the period July 1, 1976 to June 30, 1977. Included in this sum was two weeks of summer salary

plus overhead funds for Professor D. N. Seidman. The research performed with this Materials Science Center support consisted to some feasability investigations for the construction of a field-desorption microscope and some research on clustering effects in metallic glasses.

IV. LIST OF DOCUMENTS GENERATED DURING THE CONTRACT PERIOD

1. "Application of the Field-Ion and Atom-Probe Microscopes to the Study of Defects", D. N. Seidman, COO-3158-49.

2. "A Computer-Controlled Time-of-Flight Atom-Probe Field-Ion Microscope for the Study of Defects in Metals", T. M. Hall, A. Wagner and D. N. Seidman, COO-3158-50.

3. "An Atom-Probe Field-Ion Microscope for the Study of the Interaction of Impurity Atoms or Alloying Elements with Defects", A. Wagner, T. M. Hall and D. N. Seidman, COO-3158-51.

4. "The Stage II Recovery Behavior of Ion-Irradiated Pt(Au) Alloys", Ching-Yeu Wei and D. N. Seidman, COO-3158-52.

5. "A New Technique fof the Detection of Transmission Sputtering", G. Ayrault and D. N. Seidman, COO-3158-53.

6. "A Study of Low-Energy (<1keV) Transmission Sputtering in Oriented Gold Thin-Films", G. Ayrault and D. N. Seidman, COO-3158-54.

7. "A Novel Faraday Cage for the Combined Measurement and Observation of Positive-Ion Beams (300eV to 40keV)", C-Y. Wei and D. N. Seidman, COO-3158-55.

8. "A Spatial Arrangement of Vacancies in a Depleted Zone in an Ion-Irradiated Pt-4 at.% Au Alloy", C-Y. Wei and D. N. Seidman, COO-3158-56.

9. "The Study of Defects by Field-Ion and Atom-Probe Microscopy", D. N. Seidman, COO-3158-57.

10. "Annual Progress Report, "Defects in Metal Crystals", D. N. Seidman, COO-3158-58.

REFERENCES

1. R. H. Silsbee, J. Appl. Phys., 28, 1246 (1957).

2. K. H. Ecker, Rad. Effects, 23, 171 (1974).

3. F. Dworschak, H-E. Schepp and H. Wollenberger, J. Appl. Phys., 46, 1049 (1975).

4. G. K. Wehner, General Mills Report #2309 (1962); D. Rosenberg and G. K. Wehner, J. Appl. Phys., 33, 1842 (1962).

5. R. M. Scanlan, D. L. Styris, D. N. Seidman and D. G. Ast, Cornell University Materials Science Center Report #1159 (1969).

6. T. M. Hall, A. Wagner, A. S. Berger and D. N. Seidman, Cornell University Materials Science Center Report # 2357 (1975).

7. T. M. Hall, A. Wagner, A. S. Berger and D. N. Seidman, Scripta Met., 10, 485 (1976).

8. J. Moteff, V. K. Sikka and H. Jang, in Physics of Irradiation Produced Voids, (Her Majesty's Stationary Office, London, 1975) pp. 181-87.

9. B. L. Eyre, in Discussion Meeting on Defects in Refractory Metals (S.C.K./C.E.N., Mol, Belgium, 1972) pp. 311-52.

10. W. G. Johnston, T. Lauritzen, J. H. Rosolowski and A. M. Turkalo in Radiation Damage in Metals, edited by N. L. Peterson and S. D. Harkness (American Society for Metals, Metals Park, Ohio, 1976) pp. 227-66.

11. W. H. Chang and I. Perlmutter in High Temperature Materials, (Interscience, New York, 1963) pp. 347-70.

12. E. E. Bloom, J. O. Stiegler, A. F. Rowcliffe and J. M. Leitnaker, Scripta Met., 10, 303 (1976).

13. J. A. DiCarlo and J. T. Stanley in Discussion Meeting on Defects in Refractory Metals, (S.C.K./C.E.N., Mol Belgium, 1972) pp. 13-17.

14. R. M. Scanlan, D. L. Styris and D. N. Seidman, Phil. Mag., 23, 1439 (1971); R. M. Scanlan, D. L. Styris and D. N. Seidman, Phil. Mag., 23, 1459 (1971).

15. K. L. Wilson and D. N. Seidman, Radiation Effects, 27, 67 (1975).

16. D. N. Seidman, K. L. Wilson and C. H. Nielsen, Phys. Rev. Letters, 35, 1041 (1975).

17. D. N. Seidman and K. H. Lie, Acta Met., 20, 1045 (1972).

18. W. D. Wilson and C. L. Bisson, Rad. Effects, 19, 53 (1973).

19. For example see: M. Kaminsky; CRC Critical Reviews in Solid State Science, 6, 433 (1976); Proc. of 2nd Int. Conf. on Surface Effects in Controlled Fusion Devices (San Francisco, 1976); Surface Effects in Controlled Fusion, edited by H. Wiedersich, M. Kaminsky and K. M. Zwilsky (North-Holland, Amsterdam, 1974).

20. D. J. Mazey, B. L. Eyre, J. H. Evans, S. K. Erents and G. M. McCracken, AERE Report - 8140, Harwell (1976).

21. S. K. Erents and G. M. McCracken, Rad. Eff., 18, 191 (1973).

22. J. H. Evans, J. Nucl. Mat., 61, 1 (1976).

23. L. A. Beaven, R. M. Scanlan and D. N. Seidman, Acta Met., 19, 1339 (1971).

24. D. N. Seidman, J. Phys. F: Metal Phys., 3, 393 (1973).

25. K. L. Wilson and D. N. Seidman, in Defects and Defect Clusters in B.C.C. Metals and Their Alloys, Nuclear Metallurgy, Vol. 18, edited by R. J. Arsonault, University of Maryland, pp. 216-39 (1973).

26. D. N. Seidman, in Radiation Damage in Metals, edited by N. L. Peterson and S. D. Harkness (American Society for Metals, Metal Park, Ohio, 1976) pp. 28-57.

27. C. K. Johnson, Oak Ridge National Laboratory Report 3794 plus revisions (1965 and 70).

28. M. Rühle, F. Häasserman and M. Rapp, Phys. Stat. Sol., 39, 621 (1970).

29. L. A. Beavan, R. M. Scanlan and D. N. Seidman, Acta Met., 19, 1339 (1971).

30. C. A. English, B. L. Eyre, H. Wadley and A. Y. Struthopoulos, in Fundamental Aspects of Radiation Damage in Metals, edited by M. T. Robinson and F. W. Young, Jr. (National Technical Information Service, U. S. Department of Commerce, Springfield, VA, 1975) pp. 918-24.

31. M. Brumovsky in ASTM STP 570, 7 (1975).

32. C-Y. Wei and D. N. Seidman, Cornell University Materials Science Center Report #2398 (1976).

33. B. J. Shambra and J. J. Jackson, unpublished research, Argonne National Laboratory (1975).

34. W. Schilling, K. Sonnenberg and H. J. Dibbert, Rad. Effects, 16, 57 (1972).

35. M. A. Kirk, T. H. Blewitt, A. C. Klank and T. L. Scott, Argonne National Laboratory Report, Materials Science Division (1974); to appear in the Physical Review (1977).

36. R. J. Taunt, R. Sinclair and B. Ralph, Phys. Stat. Sol. (a), 16, 469 (1973).

37. B. G. LeFevre, Surface Sci., 23, 114 (1970).